

Planar Rayleigh-Taylor Instabilities – Outflows from a Binary Line-Source System

Lawrence K. Forbes
School of Mathematics and Physics
University of Tasmania
Private Bag 37, Hobart, Tasmania, AUSTRALIA. *

January 2014

Abstract

Rayleigh-Taylor instabilities occur when a light fluid lies beneath a heavier one, with an interface separating them. Under the influence of gravity, the two fluid layers attempt to exchange positions, and as a result, the interface between them is unstable, forming fingers and plumes. Here, an analogous problem is considered, but in cylindrical geometry. Two line sources are present within an inner region of lighter fluid, and each of them has an inwardly-directed gravity field. The surrounding fluid is heavier and is pushed outwards by the light inner fluid ejected from the two sources. Nonlinear inviscid solutions are calculated, and compared with the results of a linearized inviscid theory. In addition, the problem is formulated as a weakly compressible viscous outflow, and modelled with Boussinesq theory. It is found that vorticity is generated in the viscous interfacial zone, but that overturning plumes do not develop. However, the solution growth is highly sensitive to initial conditions.

Keywords: Binary sources, Boussinesq approximation, curvature singularity, Rayleigh-Taylor instability, vorticity.

*<mailto:Larry.Forbes@utas.edu.au>

1 Introduction

The Rayleigh-Taylor instability refers to the situation in which two horizontal layers of fluid are present, separated by an interface. The upper fluid is more dense than the lower one, so that any disturbance to the interface is unstable. Fingers develop as the heavier fluid punches down through the lighter one, or conversely, as bubbles of the lower lighter fluid rise upward by buoyancy. The flow was first studied theoretically by Rayleigh [1] and later by Taylor [2], using a linearized analysis in which the disturbances to the interface are considered to be small perturbations around the initial horizontal surface.

As time progresses, the interfacial disturbances eventually grow too large for the assumptions of linearized theory to remain valid. Thus, after the passage of a suitable interval of time, the shape adopted by the interface is necessarily described by non-linear equations, and may become intricate and complicated as a result. When the viscosity of the fluids is ignored, earlier computational studies observed that a time was reached at which the numerical solution abruptly failed, as discussed by Sharp [3]. The reason for this is subtle and surprising, and the phenomenon was explained by Moore [4] in a study of the Kelvin-Helmholtz instability, which is a related unstable flow that occurs when two fluids move with different speeds either side of an interface. Moore [4] showed that the curvature of the interface becomes infinite within finite time, so that inviscid models cease to be valid beyond that critical time. Moore's asymptotic theory has been confirmed and extended by Cowley, Baker and Tanveer [5]. In addition, similar asymptotic arguments were developed by Baker, Caffisch and Siegel [6] for the Rayleigh-Taylor problem, where an estimate was derived for the critical time at which a Moore curvature singularity would form at the interface, in that problem too.

When the viscosity of the fluid is taken into account, the formation of a curvature singularity at the interface within finite time is prevented. Once again, the means by which this occurs is subtle. For some time, it has been understood that viscosity permits the fluid to generate vorticity at its interface, a phenomenon not possible for purely inviscid fluids, and the result is that the interface itself may curl over into a spiral shape. One of the first methods for computing such configurations was introduced by Krasny [7], and relies on a 'vortex blob' approach, in which the interface is effectively replaced by a narrow zone of finite width in which vorticity is created, so mimicking the behaviour of a fully viscous interfacial region. Using this technique, Krasny [7] was able to obtain the famous 'cat's eye' spirals associated with the Kelvin-Helmholtz instability. Nevertheless, Baker and Pham [8] have pointed out that the details of the flow may depend to some extent

upon details of how the ‘vortex blob’ method itself is implemented, which is perhaps not surprising as these are fundamentally unstable flow situations. Forbes [9] used spectral methods to compute interface shapes in the classical planar Rayleigh-Taylor instability. In that work, it was demonstrated that the inviscid model produced a curvature singularity within finite time, but that a viscous solution then replaced that singularity with a small region of high vorticity at the interface. This occurs at precisely the time and location of the inviscid curvature singularity, and it is this effect which is responsible for the overturning of the interface and the subsequent development of spirals.

Rayleigh-Taylor flows are of interest in a wide variety of situations, and are believed to occur over vast ranges of length scales, as discussed by Kelley et al. [10]. Drips from a freshly-painted ceiling are an example of the phenomenon, and further instances are given in the review articles by Sharp [3], Kull [11] and Inogamov [12]. Flows of this type may occur on atmospheric and oceanographic length scales (see Waddell et al. [13]) and are believed to have influence even at astrophysical and galactic sizes [10]. Thus McClure-Griffiths *et al* [14] attribute certain galactic structures they observed to instances of Rayleigh-Taylor instability, and it is also proposed by Low and McCray [15] as an explanation for the structure of galactic super-bubbles.

In astrophysical situations, Rayleigh-Taylor instabilities occurring in geometries other than just the planar case may be expected to be of interest. Unstable cylindrical surfaces around line sources, or spherical surfaces of explosion or implosion, might occur in stellar flows, underwater eruptions or possibly in the inertial confinement of plasmas as indicated by Epstein [16]. In these cases, the interface is subject both to the usual Rayleigh-Taylor mechanism which results from a heavier fluid overlying a lighter one, as well as to the effects of the curvature of the interface itself. This second influence is known as the Bell-Plesset effect [16] and may act either to stabilize or destabilize the surface. The equations governing the (linear) stability of the interfacial surface in the cylindrical and the spherical cases have been presented by Mikaelian [17], and are generalized by Yu and Livescu [18] to include compressibility. More recently, Forbes [19] considered cylindrical Rayleigh-Taylor flow in the non-linear viscous and inviscid cases, for a situation in which light fluid was ejected from a line sink, into a heavier surrounding fluid. He carried out a linearized stability analysis and showed that, in the absence of gravity, his linearized equation (30) was identical to Mikaelian’s cylindrical equation (1b). Forbes [19] considered a single-mode perturbation to the cylindrical surface, as for Mikaelian’s [17] linearized analysis, and showed that this mode continues to grow as time progresses. In the inviscid case, the solution for the K -th radial mode ultimately develops cur-

vature singularities at the interface, similar to the situation discovered by Moore [4] for planar flow, and the solution fails at finite time. When viscosity is introduced, however, the K -th radial mode continues to grow, but eventually forms K overturning plumes arranged at regular intervals around the cylinder. Similar structures have been computed by Matsuoka and Nishihara [20] in a related instability (the Richtmyer-Meshkov instability).

The situation in spherical geometry turns out to be rather different to the cylindrical case. Forbes [21] examined the analogous case of outflow from a *point* source in three dimensional geometry, in which the lighter inner fluid was separated from a heavier outer fluid by an interface that was initially a *sphere*. Forbes' [21] linearized stability equation (3.12) was again identical to the corresponding equation (1c) presented for the spherical case by Mikaelian [17], but now it predicts that the lowest axi-symmetric spherical mode is the most unstable. Unlike the cylindrical case, it follows that, in spherical geometry, any perturbation is likely therefore to lead ultimately to a one-sided outflow jet, and Forbes [21] confirmed that the non-linear viscous solutions did indeed behave this way. Remarkably, one-sided outflow jets have recently been observed in astrophysics by Gómez et al. [22].

The present paper, however, is concerned with Rayleigh-Taylor type flow from a surface that is initially cylindrical, in geometry similar to that studied by Forbes [19]; the spherical case is not discussed further here. The interest here focusses instead on a *binary* system, where two line sources are present within the inner lighter fluid region. The main question of interest is whether the two sources will force the outflow to adopt a favoured shape, similar to the bi-polar morphology often encountered in astrophysics (see Stahler and Palla [23]), but in this two-dimensional flow. The spherical case does indeed favour one particular outflow shape as the likely outcome [21], although as discussed above, in that case it is uni-polar. The alternative possibility is that planar flow involving a binary source system may behave more like the single-source case [19] in which the eventual morphology is determined largely by the initial conditions for the outflow. It will be argued here that this second possibility appears the more usual outcome for planar flows involving line sinks.

In the next section 2, the inviscid model for binary outflow is presented. A spectral method for the accurate solution of this non-linear problem is also outlined, and it is based upon the technique introduced by Forbes, Chen and Trenham [24]. This approach makes use of integration by parts to derive a system of ordinary differential equations for the Fourier coefficients of the velocity potentials and interface shape, and these are then integrated forward in time from appropriate initial conditions, to give time-dependent solutions of high accuracy. The interfacial curvature is also able to be determined to

high precision from the series representations of the solution variables. A linearized solution for this inviscid model is then examined in section 3, and yields an elegant closed-form expression for the interface shape, as well as for the velocity potential in each fluid. A viscous model of this problem is also outlined in section 4, and is based upon the Boussinesq approximation, as presented by Farrow and Hocking [25]. Results obtained from the linearized and non-linear inviscid theories, and from the Boussinesq viscous model, are presented in section 5. A discussion of the work is given in section 6, along with some possible further topics for study, prompted by this analysis.

2 Inviscid Binary Outflow

Suppose that there are two inviscid incompressible fluids separated by a sharp interface. Initially, they form a circular cylinder of radius a with the light fluid of density ρ_1 inside, and the heavier fluid of density ρ_2 outside in the region $a < r < \infty$. A line source is present at the point $(x, y) = (0, b)$ inside the circular interface, so that $b < a$, and it has strength m_T (volume rate per width) and mass M_T per width. The other source is located at $(x, y) = (0, -b)$, and its strength and mass are m_B and M_B per width, respectively.

This inviscid problem will be described using cylindrical polar coordinates (r, θ) according to the usual relations $x = r \cos \theta$, $y = r \sin \theta$. The problem is also non-dimensionalized using the initial radius a of the cylinder as the characteristic length, and some reference volume rate per width m_R as a convenient measure of source outflow strength. There are thus six dimensionless parameters involved in the statement of this problem. They are

$$\begin{aligned} \beta &= \frac{b}{a} & \eta_T &= \frac{m_T}{m_R} & \eta_B &= \frac{m_B}{m_R} \\ D &= \frac{\rho_2}{\rho_1} & F_T^2 &= \frac{m_R^2}{a^2 G M_T} & F_B^2 &= \frac{m_R^2}{a^2 G M_B}. \end{aligned} \quad (1)$$

The constant β is the radius of the location of the two sources relative to the initial interface radius; since these are situated within the inner fluid, it follows that $0 < \beta < 1$. The density ratio of the outer to inner fluid is D , and for Rayleigh-Taylor flows, $D > 1$. The dimensionless strengths of the upper and lower sources are η_T and η_B respectively, and F_T and F_B are Froude numbers based on the masses of the two sources. The dimensional quantity G appearing in equations (1) is the universal gravitational constant. A sketch of the outflow geometry in non-dimensional coordinates is given in Figure 1. In fact, it would be possible to reduce by one the number of dimensionless

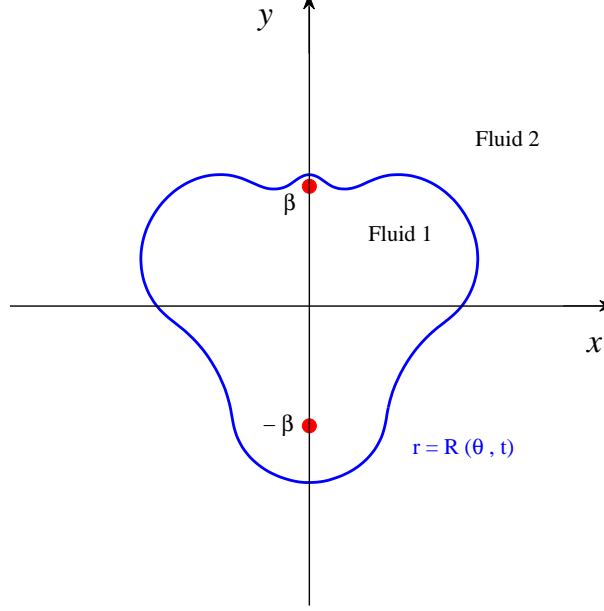


Figure 1: A sketch of the dimensionless flow configuration for the inviscid binary outflow problem. The interface is taken from an actual solution with $D = 1.05$, $F_T = F_B = 10$, $\beta = 0.8$, $\eta_T = 0.1$, $\eta_B = -0.1$ at time $t = 0.8$, and with equal scales on the two axes. The radial speed was initially perturbed at the third (odd) mode $K = 3$ with amplitude $\epsilon = 0.1$.

parameters appearing in (1), by choosing the reference source strength m_R to be either m_T or m_B . However, this has not been done here, in order to preserve the symmetry of the governing equations, as well as to allow a linearized asymptotic solution, to be presented in section 3.

Since each fluid is incompressible and inviscid, then each flows irrotationally. As a consequence, the velocity vectors $\mathbf{q}_j = u_j \mathbf{e}_r + v_j \mathbf{e}_\theta$ in each fluid may be expressed as gradients of velocity potentials Φ_j , $j = 1, 2$, so that

$$u_j = \frac{\partial \Phi_j}{\partial r} \quad ; \quad v_j = \frac{1}{r} \frac{\partial \Phi_j}{\partial \theta}. \quad (2)$$

Each velocity potential then satisfies Laplace's equation

$$\nabla^2 \Phi_j = \frac{\partial^2 \Phi_j}{\partial r^2} + \frac{1}{r} \frac{\partial \Phi_j}{\partial r} + \frac{1}{r^2} \frac{\partial^2 \Phi_j}{\partial \theta^2} = 0 \quad (3)$$

in its respective domain of validity. The two line sources are both located within the inner fluid region, and therefore

$$\begin{aligned}\Phi_1 &\rightarrow \frac{\eta_T}{2\pi} \log \sqrt{r^2 - 2\beta r \sin \theta + \beta^2} \quad \text{as } (r, \theta) \rightarrow (\beta, \pi/2) \\ \Phi_1 &\rightarrow \frac{\eta_B}{2\pi} \log \sqrt{r^2 + 2\beta r \sin \theta + \beta^2} \quad \text{as } (r, \theta) \rightarrow (\beta, -\pi/2).\end{aligned}\quad (4)$$

The two fluid regions are separated by a sharp interface, the shape of which is represented by some function $r = \mathcal{R}(\theta, t)$. Initially, the interface is simply a circle of unit dimensionless radius, so that $\mathcal{R}(\theta, 0) = 1$, but its subsequent evolution is governed by two further conditions. The first is a kinematic boundary condition, which states that neither fluid is free to cross its own boundary. It is expressed as

$$u_j = \frac{\partial \mathcal{R}}{\partial t} + \frac{v_j}{\mathcal{R}} \frac{\partial \mathcal{R}}{\partial \theta} \quad \text{on } r = \mathcal{R}(\theta, t), \quad (5)$$

and applies in each fluid at the interface, $j = 1, 2$. Secondly, there is a dynamic requirement that the pressures in each fluid must be equal at the interface. For inviscid fluids flowing irrotationally, pressure is calculated from the unsteady Bernoulli equation (see Batchelor [26], page 387), and the dynamic boundary condition may therefore be written

$$\begin{aligned}& D \frac{\partial \Phi_2}{\partial t} - \frac{\partial \Phi_1}{\partial t} + \frac{1}{2} D (u_2^2 + v_2^2) - \frac{1}{2} (u_1^2 + v_1^2) \\ & + \frac{(D-1)}{F_T^2} \log \left(\frac{\sqrt{\mathcal{R}^2 - 2\beta \mathcal{R} \sin \theta + \beta^2}}{\beta} \right) \\ & + \frac{(D-1)}{F_B^2} \log \left(\frac{\sqrt{\mathcal{R}^2 + 2\beta \mathcal{R} \sin \theta + \beta^2}}{\beta} \right) = 0 \\ & \text{on } r = \mathcal{R}(\theta, t).\end{aligned}\quad (6)$$

The two velocity potentials Φ_1 and Φ_2 and the interface profile \mathcal{R} are therefore obtained as solutions of the two Laplace equations (3), subject to the behaviour (4) of the potential in the inner fluid, along with the kinematic and dynamic boundary conditions (5) and (6).

This problem suggests naturally that a solution might be sought in terms of Fourier series. Accordingly, the spectral technique of Forbes, Chen and Trenham [24] is adapted to this cylindrical geometry, and is similar to the method used by Forbes [19] to study Rayleigh-Taylor outflow from a single source. In the inner fluid region $0 < r < \mathcal{R}(\theta, t)$, the potential is represented

as

$$\begin{aligned}\Phi_1(r, \theta, t) &= \frac{\eta_T}{2\pi} \log \sqrt{r^2 - 2\beta r \sin \theta + \beta^2} \\ &+ \frac{\eta_B}{2\pi} \log \sqrt{r^2 + 2\beta r \sin \theta + \beta^2} \\ &+ P_{1,0}(t) + \sum_{n=1}^N r^n [P_{1,n}(t) \cos(n\theta) + Q_{1,n}(t) \sin(n\theta)],\end{aligned}\quad (7)$$

and the similar relation

$$\begin{aligned}\Phi_2(r, \theta, t) &= \frac{\eta_T}{2\pi} \log \sqrt{r^2 - 2\beta r \sin \theta + \beta^2} \\ &+ \frac{\eta_B}{2\pi} \log \sqrt{r^2 + 2\beta r \sin \theta + \beta^2} \\ &+ P_{2,0}(t) + \sum_{n=1}^N r^{-n} [P_{2,n}(t) \cos(n\theta) + Q_{2,n}(t) \sin(n\theta)]\end{aligned}\quad (8)$$

is used to express the potential in the outer fluid region $r > \mathcal{R}(\theta, t)$. The shape of the interface is given by the function

$$\mathcal{R}(\theta, t) = 1 + R_0(t) + \sum_{n=1}^N [R_n(t) \cos(n\theta) + S_n(t) \sin(n\theta)].\quad (9)$$

These expressions (7)–(9) become exact as $N \rightarrow \infty$ in the upper limits of the sums, and in the numerical implementation of these formulae, N is clearly taken to be as large as is practicable.

The velocity components u_j and v_j , $j = 1, 2$ are obtained by differentiation of the forms (7), (8) according to the relations (2). These quantities are then evaluated on the interface (9), for use in the interfacial boundary conditions. The first kinematic condition, obtained with $j = 1$ in equation (5), is then subjected to standard Fourier decomposition and yields at once

$$\begin{aligned}R'_0(t) &= \frac{1}{2\pi} \int_{-\pi}^{\pi} \left[u_1 - \frac{v_1}{\mathcal{R}} \frac{\partial \mathcal{R}}{\partial \theta} \right]_{r=\mathcal{R}} d\theta \\ R'_k(t) &= \frac{1}{\pi} \int_{-\pi}^{\pi} \left[u_1 - \frac{v_1}{\mathcal{R}} \frac{\partial \mathcal{R}}{\partial \theta} \right]_{r=\mathcal{R}} \cos(k\theta) d\theta \\ S'_k(t) &= \frac{1}{\pi} \int_{-\pi}^{\pi} \left[u_1 - \frac{v_1}{\mathcal{R}} \frac{\partial \mathcal{R}}{\partial \theta} \right]_{r=\mathcal{R}} \sin(k\theta) d\theta, \\ &\text{for } k = 1, 2, \dots, N.\end{aligned}\quad (10)$$

This process therefore leads to ordinary differential equations for the Fourier coefficients in the representation (9) of the interface shape.

Following Forbes, Chen and Trenham [24], the second kinematic condition in the system (5) is replaced with the difference of these two statements, in the form

$$\mathcal{R}(u_2 - u_1) = (v_2 - v_1) \frac{\partial \mathcal{R}}{\partial \theta} \quad \text{on } r = \mathcal{R}(\theta, t). \quad (11)$$

This equation is similarly subjected to Fourier analysis. The conditions at the zeroth mode are obtained simply by integrating (11) over the interval $-\pi < \theta < \pi$, and it is found that, after the left-hand side of the equation is treated using integration by parts, the zeroth-mode condition is satisfied identically. The contribution of equation (11) at the k -th even Fourier mode is now determined by multiplying by the basis function $\cos(k\theta)$ and integrating. The left-hand side of this equation becomes

$$\begin{aligned} & \int_{-\pi}^{\pi} \mathcal{R}(u_2 - u_1)_{r=\mathcal{R}} \cos(k\theta) d\theta \\ = & \sum_{n=1}^N \int_{-\pi}^{\pi} -n\mathcal{R}^{-n} [P_{2,n}(t) \cos(n\theta) + Q_{2,n}(t) \sin(n\theta)] \cos(k\theta) d\theta \\ & -n\mathcal{R}^n [P_{1,n}(t) \cos(n\theta) + Q_{1,n}(t) \sin(n\theta)] \cos(k\theta) d\theta, \end{aligned}$$

and after integration by parts, this then takes the form

$$\begin{aligned} & \int_{-\pi}^{\pi} \mathcal{R}(u_2 - u_1)_{r=\mathcal{R}} \cos(k\theta) d\theta \\ = & \int_{-\pi}^{\pi} (v_2 - v_1)_{r=\mathcal{R}} \frac{\partial \mathcal{R}}{\partial \theta} \cos(k\theta) d\theta \\ & - k \sum_{n=1}^N \int_{-\pi}^{\pi} \mathcal{R}^{-n} [P_{2,n}(t) \sin(n\theta) - Q_{2,n}(t) \cos(n\theta)] \sin(k\theta) d\theta \\ & - k \sum_{n=1}^N \int_{-\pi}^{\pi} \mathcal{R}^n [P_{1,n}(t) \sin(n\theta) - Q_{1,n}(t) \cos(n\theta)] \sin(k\theta) d\theta. \quad (12) \end{aligned}$$

When this result (12) is incorporated into the equation giving the contribution of (11) to the k -th even mode, the algebraic system of equations

$$\begin{aligned} & \sum_{n=1}^N \int_{-\pi}^{\pi} \mathcal{R}^{-n} [P_{2,n}(t) \sin(n\theta) - Q_{2,n}(t) \cos(n\theta)] \sin(k\theta) d\theta \\ + & \sum_{n=1}^N \int_{-\pi}^{\pi} \mathcal{R}^n [P_{1,n}(t) \sin(n\theta) - Q_{1,n}(t) \cos(n\theta)] \sin(k\theta) d\theta = 0 \quad (13) \end{aligned}$$

is obtained. The similar procedure is now employed to obtain the corresponding equation for the k -th odd Fourier mode contribution from equation

(11); multiplication by the basis functions $\sin(k\theta)$ and integration by parts yields

$$\begin{aligned} & \sum_{n=1}^N \int_{-\pi}^{\pi} \mathcal{R}^{-n} [P_{2,n}(t) \sin(n\theta) - Q_{2,n}(t) \cos(n\theta)] \cos(k\theta) d\theta \\ & + \sum_{n=1}^N \int_{-\pi}^{\pi} \mathcal{R}^n [P_{1,n}(t) \sin(n\theta) - Q_{1,n}(t) \cos(n\theta)] \cos(k\theta) d\theta = 0. \end{aligned} \quad (14)$$

Although equations (13), (14) are elegant algebraic equations involving the Fourier coefficients, it is nonetheless inconvenient to retain them in this form, and ordinary differential equations for these coefficients would be preferable. As in Forbes, Chen and Trenham [24], this is achieved by direct differentiation of these equations with respect to time. A notation is first introduced for several intermediate products defined as integrals, as follows:

$$\begin{aligned} S_{1,k,n}^{CS}(t) &= \int_{-\pi}^{\pi} \mathcal{R}^n \cos(n\theta) \sin(k\theta) d\theta \\ S_{2,k,n}^{CS}(t) &= \int_{-\pi}^{\pi} \mathcal{R}^{-n} \cos(n\theta) \sin(k\theta) d\theta. \end{aligned} \quad (15)$$

There are eight families of these functions, represented as $S_{j,k,n}^{AB}$, $j = 1, 2$, in which the first exponent A is either C or S , depending on whether the second term in the integrand is $\cos(n\theta)$ or $\sin(n\theta)$. The second exponent B is likewise either C or S , corresponding to either $\cos(k\theta)$ or $\sin(k\theta)$ appearing in the third term. In terms of these intermediate functions (15), the derivatives of the even and odd components (13), (14) of the kinematic relation can be expressed in the forms

$$\begin{aligned} & \sum_{n=1}^N S_{1,k,n}^{SS} P'_{1,n}(t) - S_{1,k,n}^{CS} Q'_{1,n}(t) + S_{2,k,n}^{SS} P'_{2,n}(t) - S_{2,k,n}^{CS} Q'_{2,n}(t) \\ &= \int_{-\pi}^{\pi} \frac{\partial \mathcal{R}}{\partial t} (v_1 - v_2)_{r=\mathcal{R}} \sin(k\theta) d\theta, \quad k = 1, 2, \dots, N, \\ & \sum_{n=1}^N S_{1,k,n}^{SC} P'_{1,n}(t) - S_{1,k,n}^{CC} Q'_{1,n}(t) + S_{2,k,n}^{SC} P'_{2,n}(t) - S_{2,k,n}^{CC} Q'_{2,n}(t) \\ &= \int_{-\pi}^{\pi} \frac{\partial \mathcal{R}}{\partial t} (v_1 - v_2)_{r=\mathcal{R}} \cos(k\theta) d\theta, \quad k = 1, 2, \dots, N. \end{aligned} \quad (16)$$

The dynamic condition (6) is also subject to Fourier decomposition, in the similar manner to that applied to the kinematic conditions. The zeroth mode

term is obtained by integrating equation (6) over the interval $-\pi < \theta < \pi$. This is of little practical interest, however, since it essentially leads to a differential equation for the coefficients $P_{1,0}$ and $P_{2,0}$ in the expressions (7), (8), and these quantities can be ignored. The contributions from the higher-order even and odd Fourier modes are obtained by multiplication by basis functions $\cos(k\theta)$ and $\sin(k\theta)$, respectively, and integration over θ . This gives the further systems of differential equations

$$\begin{aligned}
& \sum_{n=1}^N -S_{1,k,n}^{CC} P'_{1,n}(t) - S_{1,k,n}^{SC} Q'_{1,n}(t) + DS_{2,k,n}^{CC} P'_{2,n}(t) + DS_{2,k,n}^{SC} Q'_{2,n}(t) \\
&= \frac{1}{2} (J_{1,k}^C - DJ_{2,k}^C) - \frac{(D-1)}{F_T^2} Y_{T,k}^C - \frac{(D-1)}{F_B^2} Y_{B,k}^C, \quad k = 1, 2, \dots, N, \\
& \sum_{n=1}^N -S_{1,k,n}^{CS} P'_{1,n}(t) - S_{1,k,n}^{SS} Q'_{1,n}(t) + DS_{2,k,n}^{CS} P'_{2,n}(t) + DS_{2,k,n}^{SS} Q'_{2,n}(t) \\
&= \frac{1}{2} (J_{1,k}^S - DJ_{2,k}^S) - \frac{(D-1)}{F_T^2} Y_{T,k}^S - \frac{(D-1)}{F_B^2} Y_{B,k}^S, \quad k = 1, 2, \dots, N \quad (17)
\end{aligned}$$

In these equations, it has proven convenient to define the additional intermediate functions

$$\begin{aligned}
J_{1,k}^C(t) &= \int_{-\pi}^{\pi} (u_1^2 + v_1^2)_{r=\mathcal{R}} \cos(k\theta) d\theta \\
Y_{T,k}^C(t) &= \int_{-\pi}^{\pi} \log \sqrt{\mathcal{R}^2 - 2\beta\mathcal{R} \sin \theta + \beta^2} \cos(k\theta) d\theta \\
Y_{B,k}^C(t) &= \int_{-\pi}^{\pi} \log \sqrt{\mathcal{R}^2 + 2\beta\mathcal{R} \sin \theta + \beta^2} \cos(k\theta) d\theta. \quad (18)
\end{aligned}$$

The superscript C in each of these functions denotes the presence of the function $\cos(k\theta)$ in the integrands, and these same quantities with an S superscript contain instead the function $\sin(k\theta)$. In the first term $J_{1,k}^C$ the subscript 1 refers to the use of the velocity components u_1 and v_1 for the inner fluid, so that replacing this with the subscript 2 indicates that the outer velocity components u_2 and v_2 are involved.

These Fourier decomposed equations now lead to an efficient numerical method for the solution of the non-linear inviscid outflow problem with the two sources. Firstly, the derivatives R'_0 , R'_k and S'_k of the Fourier coefficients for the interface shape are evaluated directly from equations (10), at each time step. Next, a coupled system of $4N$ algebraic equations is solved at each time step, to give the differentiated Fourier coefficients $P'_{1,n}$, $Q'_{1,n}$, $P'_{2,n}$, $Q'_{2,n}$. The equations involved are the Fourier decomposed kinematic

conditions (16) and dynamic conditions (17). This therefore results in a system of $6N + 1$ non-linear ordinary differential equations for the Fourier coefficients that are required to construct the solution. These equations are marched forward in time using the accurate Runge-Kutta-Fehlberg algorithm *ode45* made available in *MATLAB*.

In the evaluation of the right-hand sides of equations (10), and in the calculation of the intermediate variables (15) and (18), it is necessary to compute several integrals numerically. This is done here using Gaussian quadrature, employing the routine made available by von Winckel [27]. Accurate results are typically obtained with $N = 41$ Fourier coefficients, and 401 points placed over the interval $-\pi < \theta < \pi$ at locations determined by the requirements of the Gaussian quadrature routine of von Winckel [27].

3 Linearized Solution for the Inviscid Model

In this section, a linearized asymptotic solution is constructed to the governing equations (3)–(6), and to begin, it makes use of the Fourier-series representations (7)–(9) exactly as for the numerical solution of the non-linear problem.

Suppose that the source strengths and the gravitational attractions are all small, of the order of some small parameter ϵ , and write

$$\begin{aligned} \eta_T &= \epsilon N_T & \eta_B &= \epsilon N_B \\ \frac{1}{F_T^2} &= \epsilon S_T & \frac{1}{F_B^2} &= \epsilon S_B. \end{aligned} \quad (19)$$

The two potentials and the interface shape are now expressed as perturbations in the small parameter ϵ , and take the forms

$$\begin{aligned} \Phi_1(r, \theta, t) &= \epsilon \Phi_{1,1}(r, \theta, t) + \mathcal{O}(\epsilon^2) \\ \Phi_2(r, \theta, t) &= \epsilon \Phi_{2,1}(r, \theta, t) + \mathcal{O}(\epsilon^2) \\ \mathcal{R}(\theta, t) &= 1 + \epsilon R_1(\theta, t) + \mathcal{O}(\epsilon^2). \end{aligned} \quad (20)$$

These approximations (19), (20) are substituted into the governing inviscid equations and terms retained at the first order in the small parameter ϵ .

The perturbation potential $\Phi_{1,1}$ is found to obey Laplace's equation (3) within the undeformed inner region $0 < r < 1$. Similarly, $\Phi_{2,1}$ satisfies Laplace's equation in the undisturbed outer zone $r > 1$. Near the two line

sources, equations (4) take the linearized forms

$$\begin{aligned}\Phi_{1,1} &\rightarrow \frac{N_T}{2\pi} \log \sqrt{r^2 - 2\beta r \sin \theta + \beta^2} \quad \text{as } (r, \theta) \rightarrow (\beta, \pi/2) \\ \Phi_{1,1} &\rightarrow \frac{N_B}{2\pi} \log \sqrt{r^2 + 2\beta r \sin \theta + \beta^2} \quad \text{as } (r, \theta) \rightarrow (\beta, -\pi/2),\end{aligned}\quad (21)$$

and the two kinematic conditions (5) become approximately

$$\frac{\partial \Phi_{1,1}}{\partial r} = \frac{\partial R_1}{\partial t} \quad ; \quad \frac{\partial \Phi_{2,1}}{\partial r} = \frac{\partial R_1}{\partial t} \quad \text{on } r = 1. \quad (22)$$

Finally, the dynamic condition (6) linearizes to

$$\begin{aligned}& D \frac{\partial \Phi_{2,1}}{\partial t} - \frac{\partial \Phi_{1,1}}{\partial t} \\ & + (D-1)S_T \log \left(\frac{\sqrt{1 - 2\beta \sin \theta + \beta^2}}{\beta} \right) \\ & + (D-1)S_B \log \left(\frac{\sqrt{1 + 2\beta \sin \theta + \beta^2}}{\beta} \right) = 0 \quad \text{on } r = 1.\end{aligned}\quad (23)$$

These linearized equations may now be solved using the same forms (7), (8) derived for the non-linear solution, provided that Φ_1 and Φ_2 are replaced with the perturbation potentials $\Phi_{1,1}$ and $\Phi_{2,1}$ and source strengths η_T and η_B are replaced with their linearized counterparts N_T and N_B . The zeroth-order coefficients $P_{1,0}$ and $P_{2,0}$ play no role in the linearized solution and so will be ignored.

It follows at once from the difference of the two linearized kinematic conditions (22) that

$$P_{2,n} = -P_{1,n} \quad ; \quad Q_{2,n} = -Q_{1,n} \quad , n \geq 1. \quad (24)$$

The linearized dynamic condition (23) is Fourier analyzed, exactly as in the algorithm developed in Section 2 for the non-linear problem, by multiplying by basis functions $\cos(k\theta)$ and $\sin(k\theta)$ and integrating once around the circle $r = 1$. After making use of the relations (24), it follows that

$$\begin{aligned}P'_{1,k} &= \frac{(D-1)(S_T + S_B)}{\pi(D+1)} \mathcal{C}_k(\beta) \\ Q'_{1,k} &= \frac{(D-1)(S_T - S_B)}{\pi(D+1)} \mathcal{S}_k(\beta), \quad , k \geq 1,\end{aligned}\quad (25)$$

in which it is convenient to define constants

$$\begin{aligned}\mathcal{C}_k(\beta) &= \int_{-\pi}^{\pi} \cos(k\theta) \log \sqrt{1 - 2\beta \sin \theta + \beta^2} d\theta \\ \mathcal{S}_k(\beta) &= \int_{-\pi}^{\pi} \sin(k\theta) \log \sqrt{1 - 2\beta \sin \theta + \beta^2} d\theta.\end{aligned}\quad (26)$$

The interfacial shape can be recovered from (22), and gives

$$\begin{aligned}R_1(\theta, t) &= t \frac{N_T}{2\pi} \frac{(1 - \beta \sin \theta)}{(1 - 2\beta \sin \theta + \beta^2)} + t \frac{N_B}{2\pi} \frac{(1 + \beta \sin \theta)}{(1 + 2\beta \sin \theta + \beta^2)} \\ &+ \frac{t^2}{2\pi} \frac{(D-1)}{(D+1)} \sum_{n=1}^{\infty} n \left[(S_T + S_B) \mathcal{C}_n(\beta) \cos(n\theta) \right. \\ &\quad \left. + (S_T - S_B) \mathcal{S}_n(\beta) \sin(n\theta) \right]\end{aligned}\quad (27)$$

in the linearized theory. Here, it has been assumed that the interface was the circle $r = 1$ at time $t = 0$, so that the perturbation function in equation (20) took the initial value $R_1(\theta, 0) = 0$.

Integration by parts allows the intermediate constants in equation (26) to be expressed as

$$\begin{aligned}\mathcal{C}_n(\beta) &= \frac{\beta}{n} \int_{-\pi}^{\pi} \frac{\cos \theta \sin(n\theta)}{1 - 2\beta \sin \theta + \beta^2} d\theta \\ \mathcal{S}_n(\beta) &= -\frac{\beta}{n} \int_{-\pi}^{\pi} \frac{\cos \theta \cos(n\theta)}{1 - 2\beta \sin \theta + \beta^2} d\theta.\end{aligned}\quad (28)$$

It turns out that, when expressed in the form (28), these integrals may be evaluated in closed form, using the calculus of residues. Further details are given in the Appendix 7. The final expressions take the remarkably simple forms

$$\begin{aligned}\mathcal{C}_n(\beta) &= -\frac{\pi \beta^n}{n} \cos\left(\frac{n\pi}{2}\right) \\ \mathcal{S}_n(\beta) &= -\frac{\pi \beta^n}{n} \sin\left(\frac{n\pi}{2}\right).\end{aligned}\quad (29)$$

When these forms (29) are used in the expressions for the interface shape,

then equations (27), (19), (20) and a little algebra give the linearized interface

$$\begin{aligned}
R(\theta, t) = 1 &+ t \frac{\eta_T}{2\pi} \frac{(1 - \beta \sin \theta)}{(1 - 2\beta \sin \theta + \beta^2)} + t \frac{\eta_B}{2\pi} \frac{(1 + \beta \sin \theta)}{(1 + 2\beta \sin \theta + \beta^2)} \\
&- \frac{t^2 (D-1)}{2(D+1)} \sum_{n=1}^{\infty} \left[\frac{1}{F_T^2} \beta^n \cos(n(\theta - \pi/2)) \right. \\
&\quad \left. + \frac{1}{F_B^2} \beta^n \cos(n(\theta + \pi/2)) \right] + \mathcal{O}(\epsilon^2).
\end{aligned}$$

It turns out that the sums in this expression can be evaluated in closed form. Each of them is an expression of the form

$$\sum_{n=1}^{\infty} \beta^n \cos(n\phi) = \text{Re} \left\{ \sum_{n=1}^{\infty} \beta^n e^{in\phi} \right\}$$

with $0 < \beta < 1$, and so can be evaluated as a geometric sum. Taking the real part of the resulting expression then gives

$$\sum_{n=1}^{\infty} \beta^n \cos(n\phi) = -\beta \left[\frac{\beta - \cos \phi}{1 - 2\beta \cos \phi + \beta^2} \right].$$

As a result, the linearized expression for the interface shape takes the final form

$$\begin{aligned}
R(\theta, t) = 1 &+ t \frac{\eta_T}{2\pi} \frac{(1 - \beta \sin \theta)}{(1 - 2\beta \sin \theta + \beta^2)} \\
&+ t \frac{\eta_B}{2\pi} \frac{(1 + \beta \sin \theta)}{(1 + 2\beta \sin \theta + \beta^2)} \\
&+ \frac{\beta t^2}{2F_T^2} \left(\frac{D-1}{D+1} \right) \left(\frac{\beta - \sin \theta}{1 - 2\beta \sin \theta + \beta^2} \right) \\
&+ \frac{\beta t^2}{2F_B^2} \left(\frac{D-1}{D+1} \right) \left(\frac{\beta + \sin \theta}{1 + 2\beta \sin \theta + \beta^2} \right) + \mathcal{O}(\epsilon^2). \quad (30)
\end{aligned}$$

The potentials in each fluid region are now considered. From equations (19) and (20), it is possible to write

$$\begin{aligned}
\Phi_1(r, \theta, t) &= \frac{\eta_T}{2\pi} \log \sqrt{r^2 - 2\beta r \sin \theta + \beta^2} \\
&+ \frac{\eta_B}{2\pi} \log \sqrt{r^2 + 2\beta r \sin \theta + \beta^2} \\
&+ \sum_{n=1}^{\infty} r^n [\epsilon P_{1,n} \cos(n\theta) + \epsilon Q_{1,n} \sin(n\theta)] \\
&+ \mathcal{O}(\epsilon^2), \quad \text{in } 0 < r < 1 \quad (31)
\end{aligned}$$

and

$$\begin{aligned}
\Phi_2(r, \theta, t) &= \frac{\eta_T}{2\pi} \log \sqrt{r^2 - 2\beta r \sin \theta + \beta^2} \\
&+ \frac{\eta_B}{2\pi} \log \sqrt{r^2 + 2\beta r \sin \theta + \beta^2} \\
&+ \sum_{n=1}^{\infty} r^{-n} [\epsilon P_{2,n} \cos(n\theta) + \epsilon Q_{2,n} \sin(n\theta)] \\
&+ \mathcal{O}(\epsilon^2), \quad \text{in } r > 1.
\end{aligned} \tag{32}$$

The coefficients in (31) are determined to be

$$\begin{aligned}
\epsilon P_{1,n}(t) &= \frac{t}{\pi} \left(\frac{D-1}{D+1} \right) \left(\frac{1}{F_T^2} + \frac{1}{F_B^2} \right) \mathcal{C}_n(\beta) \\
\epsilon Q_{1,n}(t) &= \frac{t}{\pi} \left(\frac{D-1}{D+1} \right) \left(\frac{1}{F_T^2} - \frac{1}{F_B^2} \right) \mathcal{S}_n(\beta),
\end{aligned} \tag{33}$$

and those in (32) are evaluated in terms of these using equation (24). The constants \mathcal{C}_n and \mathcal{S}_n are given in equation (29), and when these are incorporated into (33), the expression (31) takes the form

$$\begin{aligned}
\Phi_1(r, \theta, t) &= \frac{\eta_T}{2\pi} \log \sqrt{r^2 - 2\beta r \sin \theta + \beta^2} \\
&+ \frac{\eta_B}{2\pi} \log \sqrt{r^2 + 2\beta r \sin \theta + \beta^2} \\
&- t \left(\frac{D-1}{D+1} \right) \sum_{n=1}^{\infty} \frac{1}{n} (r\beta)^n \left[\frac{1}{F_T^2} \cos(n(\theta - \pi/2)) + \frac{1}{F_B^2} \cos(n(\theta + \pi/2)) \right] \\
&+ \mathcal{O}(\epsilon^2), \quad \text{in } 0 < r < 1.
\end{aligned} \tag{34}$$

The series in this expression is able to be evaluated in closed form, and to do this, it is first necessary to consider

$$\sum_{n=1}^{\infty} (r\beta)^n \sin(n\xi) = \text{Im} \left\{ \sum_{n=0}^{\infty} (r\beta)^n e^{in\xi} \right\}.$$

Since $0 < r\beta < 1$, this may be evaluated at once as a geometric sum, and after taking the imaginary part, gives the result

$$\sum_{n=1}^{\infty} (r\beta)^n \sin(n\xi) = \frac{\beta r \sin \xi}{1 - 2\beta r \cos \xi + \beta^2 r^2}. \tag{35}$$

Now the sums in the representation (34) may formally be associated with indefinite integrals of (35), so that

$$\begin{aligned}
& - \sum_{n=1}^{\infty} \frac{1}{n} (r\beta)^n \cos(n\xi) \\
& = \int \sum_{n=1}^{\infty} (r\beta)^n \sin(n\xi) d\xi \\
& = \log \sqrt{1 - 2\beta r \cos \xi + \beta^2 r^2}.
\end{aligned}$$

Consequently, the final form of the linearized expression for the potential in the inner fluid becomes

$$\begin{aligned}
\Phi_1(r, \theta, t) &= \frac{\eta_T}{2\pi} \log \sqrt{r^2 - 2\beta r \sin \theta + \beta^2} \\
&+ \frac{\eta_B}{2\pi} \log \sqrt{r^2 + 2\beta r \sin \theta + \beta^2} \\
&+ t \left(\frac{D-1}{D+1} \right) \left[\frac{1}{F_T^2} \log \sqrt{1 - 2\beta r \sin \theta + \beta^2 r^2} \right. \\
&\quad \left. + \frac{1}{F_B^2} \log \sqrt{1 + 2\beta r \sin \theta + \beta^2 r^2} \right] \\
&+ \mathcal{O}(\epsilon^2), \quad \text{in } 0 < r < 1.
\end{aligned} \tag{36}$$

This is a remarkable simplification, and it demonstrates that the linearized potential for the fluid in the inner layer consists of the two sources (21) at $(r, \theta) = (\beta, \pm\pi/2)$, and two image sources outside the domain, at points $(r, \theta) = (1/\beta, \pm\pi/2)$ and with strengths proportional to the gravitational strengths of the two line sources but increasingly linearly with time t .

A similar process may be carried out for the linearized potential Φ_2 in equation (32). After some algebra, the final form of this expression becomes

$$\begin{aligned}
\Phi_2(r, \theta, t) &= \frac{\eta_T}{2\pi} \log \sqrt{r^2 - 2\beta r \sin \theta + \beta^2} \\
&+ \frac{\eta_B}{2\pi} \log \sqrt{r^2 + 2\beta r \sin \theta + \beta^2} \\
&- t \left(\frac{D-1}{D+1} \right) \left[\frac{1}{F_T^2} \log \sqrt{r^2 - 2\beta r \sin \theta + \beta^2} \right. \\
&\quad \left. + \frac{1}{F_B^2} \log \sqrt{r^2 + 2\beta r \sin \theta + \beta^2} \right] \\
&+ \mathcal{O}(\epsilon^2), \quad \text{in } r > 1.
\end{aligned} \tag{37}$$

Thus the outer potential Φ_2 creates two further image sources at the locations $(r, \theta) = (\beta, \pm\pi/2)$ of the actual sources, exterior to the outer region, and

again with strengths proportional to the gravitational source strength and increasing linearly with time t . The constant $(D - 1)/(D + 1)$ in equations (36), (37) is the Atwood number familiar in the literature on the Rayleigh-Taylor instability [3].

In summary, the linearized potentials in the two fluid layers are given by the simple closed-form expressions (36) and (37), correct to second order in the small parameter ϵ . They infer the linearized interface shape (30) in inviscid theory.

4 Boussinesq Model for Viscous Binary Outflow

Following Farrow and Hocking [25], a viscous model is also formulated for this problem, using the Boussinesq approximation to simplify the otherwise complex task of treating the exact interface. This same approximation has also been used by Forbes [19] to study outflow from a single line source in planar flow, and it was found there that overturning viscous plumes could be formed at the interface, sometimes in a ring surrounding the line source. The interface is approximated by a narrow region in which the density changes continuously but rapidly from the value ρ_2 far away to the lesser amount ρ_1 inside the interfacial zone. This is achieved by representing the dimensional fluid density as $\rho = \rho_2 + \bar{\rho}$ and requiring that the perturbation density $\bar{\rho}$ be assumed small relative to ρ_2 .

In the corresponding non-dimensionalized variables introduced in Section 2, the length scale is again taken to be the initial circle radius a of the inner bubble, and the scale for volume rate per width is some quantity m_R . Time is referenced to a^2/m_R . The flow is no longer irrotational, as for the inviscid model in section 2, and so a velocity potential does not exist here; nevertheless, a streamfunction Ψ may be constructed, and it is made dimensionless using the quantity m_R . A vorticity will be introduced as the vector curl of the fluid velocity, and then non-dimensionalized by reference to m_R/a^2 . Finally the density is measured relative to the inner amount ρ_1 so that the dimensionless quantity $\bar{\rho}$ becomes zero far away and takes the value $-(D - 1)$ inside the bubble. In addition to the parameters defined in equation (1), the two additional quantities σ and $R_e = \rho_1 m_R / \mu$ are also needed here. The first of these is a diffusion constant for the density perturbation $\bar{\rho}$ and R_e is a Reynolds number in which μ is the (dimensional) dynamic viscosity of the fluid.

Due to the presence of *two* singularities, there is no particular advantage

in retaining the polar coordinates of Section 2, so that the usual cartesian (x, y) system will be used instead, in this viscous model. The velocity vector is therefore expressed as $\mathbf{q} = u\mathbf{i} + v\mathbf{j}$, with the two velocity components calculated from the streamfunction according to the usual relations

$$u = \frac{\partial \Psi}{\partial y} \quad ; \quad v = -\frac{\partial \Psi}{\partial x}, \quad (38)$$

replacing equation (2) in Section 2. The vorticity vector has only the single component ζ in a direction normal to the $x - y$ plane; it is obtained by taking curl of the velocity vector \mathbf{q} and gives

$$\zeta = \frac{\partial v}{\partial x} - \frac{\partial u}{\partial y} = -\nabla^2 \Psi, \quad (39)$$

in which the symbol ∇^2 denotes the Laplacian. Near the two sources, the streamfunction behaves like

$$\begin{aligned} \Psi &\rightarrow \frac{\eta_T}{2\pi} \arctan\left(\frac{y - \beta}{x}\right) \quad \text{as } (x, y) \rightarrow (0, \beta) \\ \Psi &\rightarrow \frac{\eta_B}{2\pi} \arctan\left(\frac{y + \beta}{x}\right) \quad \text{as } (x, y) \rightarrow (0, -\beta). \end{aligned} \quad (40)$$

The Boussinesq approach is essentially a weakly compressible approximation, in which the usual mass continuity equation is “split” into an incompressible component $\text{div} \mathbf{q} = 0$ and a transport equation

$$\frac{\partial \bar{\rho}}{\partial t} + u \frac{\partial \bar{\rho}}{\partial x} + v \frac{\partial \bar{\rho}}{\partial y} = \sigma \left[\frac{\partial^2 \bar{\rho}}{\partial x^2} + \frac{\partial^2 \bar{\rho}}{\partial y^2} \right] \quad (41)$$

for the perturbation density $\bar{\rho}$. The incompressible component is satisfied by the identities (38), but the weakly compressible approximation (41) must be treated explicitly.

In dimensionless coordinates, the Boussinesq-Navier-Stokes momentum equation takes the form

$$\begin{aligned} &D \frac{\partial \mathbf{q}}{\partial t} + D(\mathbf{q} \cdot \nabla) \mathbf{q} + \nabla p \\ &= -\frac{1}{F_T^2} (D + \bar{\rho}) \frac{x\mathbf{i} + (y - \beta)\mathbf{j}}{x^2 + (y - \beta)^2} \\ &\quad - \frac{1}{F_B^2} (D + \bar{\rho}) \frac{x\mathbf{i} + (y + \beta)\mathbf{j}}{x^2 + (y + \beta)^2} + \frac{1}{R_e} \nabla^2 \mathbf{q}. \end{aligned} \quad (42)$$

The vector curl of this equation (42) is now taken, and gives a vorticity equation with only one component in the direction orthogonal to the $x - y$ plane. The result is

$$\begin{aligned}
& \frac{\partial \zeta}{\partial t} + u \frac{\partial \zeta}{\partial x} + v \frac{\partial \zeta}{\partial y} \\
&= -\frac{1}{DF_T^2} \frac{1}{[x^2 + (y - \beta)^2]} \left[(y - \beta) \frac{\partial \bar{\rho}}{\partial x} - x \frac{\partial \bar{\rho}}{\partial y} \right] \\
&\quad -\frac{1}{DF_B^2} \frac{1}{[x^2 + (y + \beta)^2]} \left[(y + \beta) \frac{\partial \bar{\rho}}{\partial x} - x \frac{\partial \bar{\rho}}{\partial y} \right] \\
&\quad + \frac{1}{DR_e} \left(\frac{\partial^2 \zeta}{\partial x^2} + \frac{\partial^2 \zeta}{\partial y^2} \right), \tag{43}
\end{aligned}$$

where ζ is as defined in equation (39).

The solution to this Boussinesq viscous problem thus involves finding functions Ψ , $\bar{\rho}$ and ζ satisfying the three equations (39), (41) and (43), subject to the conditions (40) near the two line sources. From the numerical standpoint, it is necessary to define a computational window $-L < x < L$, $-B < y < B$ in the plane; in this paper, as in the earlier studies [9], [19], a spectral method will be used, in which the streamfunction is represented as

$$\begin{aligned}
\Psi(x, y, t) &= \frac{\eta_T}{2\pi} \arctan\left(\frac{y - \beta}{x}\right) + \frac{\eta_B}{2\pi} \arctan\left(\frac{y + \beta}{x}\right) \\
&+ \sum_{m=1}^M \sum_{n=1}^N A_{mn}(t) \sin\left(\frac{m\pi(x + L)}{2L}\right) \sin\left(\frac{n\pi(y + B)}{2B}\right). \tag{44}
\end{aligned}$$

In this expression, the time-dependent Fourier coefficients $A_{mn}(t)$ are to be determined. The two velocity components u and v in the x - and y -directions are obtained from (44) by exact differentiation of this expression, according to equation (38), and the definition (39) of vorticity then gives

$$\zeta(x, y, t) = \sum_{m=1}^M \sum_{n=1}^N C_{mn} A_{mn}(t) \sin\left(\frac{m\pi(x + L)}{2L}\right) \sin\left(\frac{n\pi(y + B)}{2B}\right) \tag{45}$$

as the appropriate representation of that variable. The auxiliary constants in this expression are defined to be

$$C_{mn} = \left(\frac{m\pi}{2L}\right)^2 + \left(\frac{n\pi}{2B}\right)^2. \tag{46}$$

Finally, a representation is needed for the perturbation density $\bar{\rho}$. The form of this function must be consistent with that assumed for the vorticity (45),

since these two quantities are coupled through the buoyancy term in the vorticity equation (43). It is appropriate to take

$$\bar{\rho}(x, y, t) = \sum_{m=0}^M \sum_{n=0}^N R_{mn}(t) \cos\left(\frac{m\pi(x+L)}{2L}\right) \cos\left(\frac{n\pi(y+B)}{2B}\right), \quad (47)$$

in which the time-dependent Fourier coefficients $R_{mn}(t)$ are also to be found.

The presence of *two* singularities within the fluid region poses a significant numerical challenge, and one not encountered in the earlier study [19] in which only the one line sink was involved. When spectral methods are used, the solution technique works by multiplying the governing equations by the basis functions used in the representations (45), (47) and then integrating over the chosen computational domain. Typically, elegant orthogonality conditions can be brought to bear, so that the resulting equation reduces to differential equations for the derivatives $A'_{mn}(t)$ or $R'_{mn}(t)$ of the appropriate Fourier coefficients; these may then be integrated forward in time to yield the solution. However, when this is done in the present problem, the singularities (40) at the two sources within the fluid give rise to certain integrals that no longer converge, so that the spectral method is invalid. To overcome this difficulty, each equation is first multiplied by the weight function $[x^2 + (y - \beta)^2][x^2 + (y + \beta)^2]$. This has the effect of neutralizing the singularities at the points $(x, y) = (0, \pm\beta)$. Now spectral methods may again be used, but at the cost of losing the use of orthogonality conditions. Consequently, a full matrix equation must be solved at each time step of the numerical solution technique, which may significantly increase the computational cost of the method.

Under this approach, the density equation (41) yields the system

$$\sum_{m=0}^M \sum_{n=0}^N G_{mnk\ell} [R'_{mn}(t) + \sigma C_{mn} R_{mn}(t)] = -E_{k\ell} \quad (48)$$

$$k = 0, 1, \dots, M, \quad \ell = 0, 1, \dots, N$$

of $(M+1)(N+1)$ differential equations for the Fourier coefficients $R_{mn}(t)$. The matrix coefficients in this expression are defined as

$$\begin{aligned} G_{mnk\ell}(t) = & \int_{-L}^L \int_{-B}^B [x^2 + (y - \beta)^2][x^2 + (y + \beta)^2] \\ & \times \cos\left(\frac{m\pi(x+L)}{2L}\right) \cos\left(\frac{k\pi(x+L)}{2L}\right) \\ & \times \cos\left(\frac{n\pi(y+B)}{2B}\right) \cos\left(\frac{\ell\pi(y+B)}{2B}\right) dy dx \\ & m, k = 0, 1, \dots, M, \quad n, \ell = 0, 1, \dots, N \end{aligned} \quad (49)$$

and the functions on the right-hand side are given by the expression

$$\begin{aligned}
E_{k\ell}(t) &= \int_{-L}^L \int_{-B}^B [x^2 + (y - \beta)^2] [x^2 + (y + \beta)^2] \\
&\quad \times \left(u \frac{\partial \bar{\rho}}{\partial x} + v \frac{\partial \bar{\rho}}{\partial y} \right) \cos\left(\frac{k\pi(x+L)}{2L}\right) \cos\left(\frac{\ell\pi(y+B)}{2B}\right) dy dx \\
&\quad k = 0, 1, \dots, M, \quad \ell = 0, 1, \dots, N.
\end{aligned} \tag{50}$$

A similar treatment of the vorticity equation (43) gives rise to the further system

$$\begin{aligned}
\sum_{m=1}^M \sum_{n=1}^N H_{mnk\ell} C_{mn} [A'_{mn}(t) + \frac{1}{DR_e} C_{mn} A_{mn}(t)] &= -F_{k\ell} \\
k = 1, \dots, M, \quad \ell = 1, \dots, N.
\end{aligned} \tag{51}$$

This constitutes MN additional ordinary differential equations for the Fourier coefficients $A_{mn}(t)$. In this expression, the matrix coefficients are

$$\begin{aligned}
H_{mnk\ell}(t) &= \int_{-L}^L \int_{-B}^B [x^2 + (y - \beta)^2] [x^2 + (y + \beta)^2] \\
&\quad \times \sin\left(\frac{m\pi(x+L)}{2L}\right) \sin\left(\frac{k\pi(x+L)}{2L}\right) \\
&\quad \times \sin\left(\frac{n\pi(y+B)}{2B}\right) \sin\left(\frac{\ell\pi(y+B)}{2B}\right) dy dx \\
&\quad m, k = 1, \dots, M, \quad n, \ell = 1, \dots, N.
\end{aligned} \tag{52}$$

The functions on the right-hand side of equation (51) are

$$\begin{aligned}
F_{k\ell}(t) &= \int_{-L}^L \int_{-B}^B \left\{ [x^2 + (y - \beta)^2] [x^2 + (y + \beta)^2] \left(u \frac{\partial \zeta}{\partial x} + v \frac{\partial \zeta}{\partial y} \right) \right. \\
&\quad + \frac{1}{DF_T^2} [x^2 + (y + \beta)^2] \left[(y - \beta) \frac{\partial \bar{\rho}}{\partial x} - x \frac{\partial \bar{\rho}}{\partial y} \right] \\
&\quad + \frac{1}{DF_B^2} [x^2 + (y - \beta)^2] \left[(y + \beta) \frac{\partial \bar{\rho}}{\partial x} - x \frac{\partial \bar{\rho}}{\partial y} \right] \Big\} \\
&\quad \times \sin\left(\frac{k\pi(x+L)}{2L}\right) \sin\left(\frac{\ell\pi(y+B)}{2B}\right) dy dx \\
&\quad k = 1, \dots, M, \quad \ell = 1, \dots, N.
\end{aligned} \tag{53}$$

The constants C_{mn} in equations (48) and (51) are as defined in equation (46).

Initial conditions must be chosen for this viscous problem. For now, the velocity components are taken to be just those given by the two sources, so that the coefficients are given the starting values $A_{mn}(0) = 0$ in the representations (44), (45), although different starting conditions will be examined later. The density perturbation at time $t = 0$ is

$$\bar{\rho}(r, \theta, 0) = \begin{cases} -(D - 1), & \text{for } x^2 + y^2 < 1 \\ 0, & \text{otherwise,} \end{cases} \quad (54)$$

representing an effective circular interface of unit radius between the two fluids. It follows from the representation (47) that

$$\begin{aligned} R_{mn}(0) = & \frac{1}{[1 + \delta_{m0}][1 + \delta_{n0}]LB} \int_{-L}^L \int_{-B}^B \bar{\rho}(r, \theta, 0) \\ & \times \cos\left(\frac{m\pi(x+L)}{2L}\right) \cos\left(\frac{n\pi(y+B)}{2B}\right) dy dx \\ & m = 0, 1, \dots, M, \quad n = 0, 1, \dots, N. \end{aligned} \quad (55)$$

In this expression, the Kronecker delta symbol takes the values $\delta_{m0} = 1$ if $m = 0$ and zero for all integers $m \neq 0$. Similarly, $\delta_{n0} = 1$ for $n = 0$ and is zero otherwise.

The algorithm for the solution of this viscous problem thus proceeds as follows. To begin, initial values of the Fourier coefficients $A_{mn}(0) = 0$ are given, and $R_{mn}(0)$ are computed numerically from equation (55) using the function (54). The numerical quadratures in (55), as well as in the intermediate products (49), (50) and (52), (53), are evaluated to very high accuracy using the Gauss-Legendre integration routine provided by von Winckel [27]. Equations (48) and (51) constitute a system of $2MN + M + N + 1$ ordinary differential equations for the Fourier coefficients, to be integrated forward in time. At each new time step, the matrix equation (48) is solved, and then rearranged to obtain the derivatives R'_{mn} . Similarly, equation (51) is inverted and then rearranged to give A'_{mn} . These derivatives R'_{mn} and A'_{mn} are stored in a vector of length $2MN + M + N + 1$ and the *MATLAB* Runge-Kutta-Fehlberg routine *ode45* is used to advance the solution forward in time. This is done using two embedded loops, to enable the solution variables to be re-created from their Fourier representations (44), (45) at certain times of interest. The algorithm is made very greatly more efficient by caching the trigonometric functions $\cos(m\pi(x+L)/(2L))$, and so on, at the beginning of the run, so that they are not re-computed. In addition, the matrix elements $G_{mnk\ell}$ and $H_{mnk\ell}$ in equations (49) and (52) are then calculated once at the outset and stored, since they are time-independent quantities. In this way,

although the algorithm is unable to take advantage of the orthogonality of the trigonometric functions and must instead solve the full matrix equations (48) and (51) at each time step, the computational cost of this is reduced just to a fixed overhead at the beginning of the run.

The results to be presented in this paper have typically used 91 mesh points in x and 151 points in y , with a computational domain defined by the constants $L = 3$ and $B = 5$. With this number of grid points, the numerical quadratures in the algorithm are performed to extremely high precision, so that the only significant numerical error arises from the numbers M, N of Fourier coefficients chosen. It has been found by experimentation that $M = 25, N = 41$ coefficients is sufficient to give converged numerical results over the time intervals of practical interest.

5 Presentation of Results

A large number of runs has been made, to map out the solution behaviour over a range of the dimensionless parameters. A representative sample of these results is discussed here. For convenience, the density ratio will be taken to be $D = 1.05$, consistently with the Boussinesq approximation. In addition, for the linearized solution of section 3 to be valid, the inverse Froude numbers and source strength magnitudes must be small, consistently with equation (19). In order to facilitate comparison with the linearized result, the Froude numbers will therefore be set to the values $F_T = F_B = 10$. Although many values of the source off-set parameter β have been investigated, here only the value $\beta = 0.8$ will be discussed.

Figure 2 shows a comparison of the predictions of the linearized theory (30) with the corresponding non-linear inviscid theory of section 2. Here, sources of equal strength $\eta_T = \eta_B = 0.1$ are present at the locations $(x, y) = (0, \pm 0.8)$ and are indicated with small circles on the diagram. Solutions are shown at the early time $t = 2$ and a rather later time $t = 10$. The solution starts from a circular interface of radius $\mathcal{R} = 1$ at $t = 0$, and there is good agreement between the linearized and non-linear solutions at early times. Thus the two solutions at $t = 2$ in Figure 2 are almost identical, except for the two small regions near the poles, where the linearized solution is slightly in excess of the non-linear one. As time continues, the linearized solution necessarily becomes less reliable, since it has been derived on the assumption that the deviation from a unit circle is only ever slight; this fails to be true when there are two sources present, driving a continual outflow. The two solutions at the later time $t = 10$ illustrate this effect, since the linearized solution clearly over-estimates the extent of the bulge in the interface near

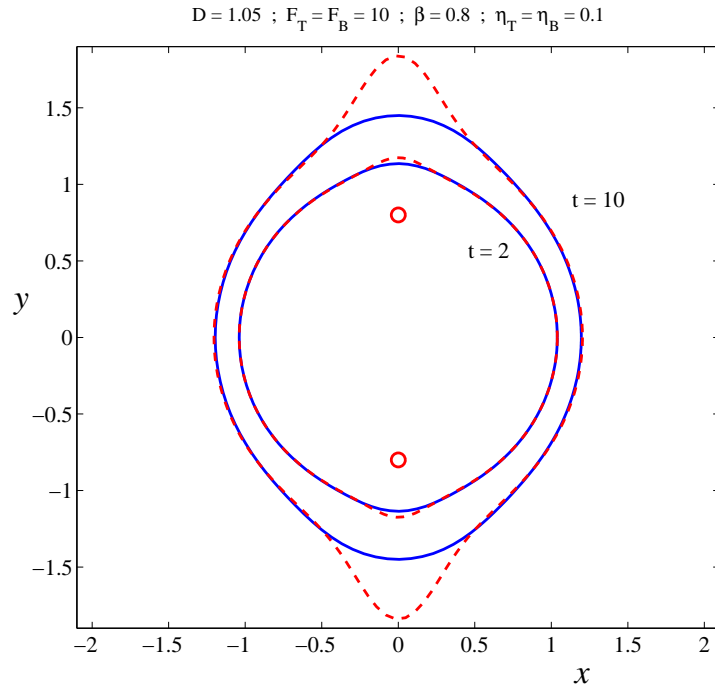


Figure 2: The inviscid solution for two different times $t = 2$ and $t = 10$, obtained from the linearized (red, dashed line) and non-linear (blue, solid line) solutions of sections 3 and 2, respectively. Here, $D = 1.05$, $F_T = F_B = 10$, $\beta = 0.8$, $\eta_T = \eta_B = 0.1$, and the scales on the two axes are equal. The two small red circles indicate the locations of the two sources.

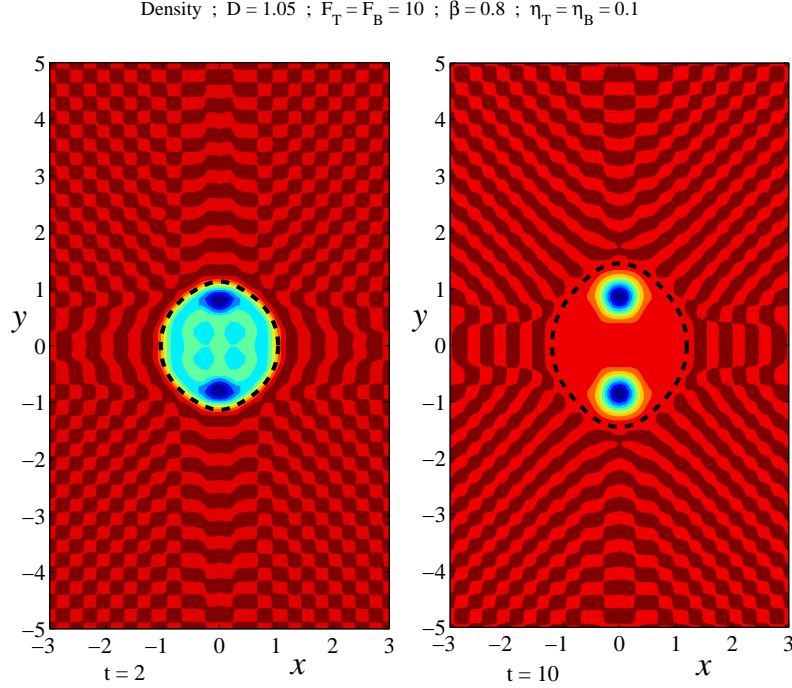


Figure 3: Density contours for the viscous Boussinesq solution, at the two different times $t = 2$ and $t = 10$. The non-linear inviscid solution is overlaid on these diagrams, and is indicated with a heavy dashed line. Here, $D = 1.05$, $F_T = F_B = 10$, $\beta = 0.8$, $\eta_T = \eta_B = 0.1$, and the scales on the axes are equal.

the two poles on the y - axis.

The non-linear inviscid solutions in Figure 2 are contrasted against the predictions of the viscous Boussinesq theory of section 4, in Figure 3. Here, contours of the perturbation density $\bar{\rho}$ are plotted at the same two times $t = 2$ and $t = 10$. The non-linear inviscid interfaces are then superposed on these diagrams as heavy dashed lines. In both these images, the viscous density perturbation function $\bar{\rho}$ is essentially zero in the outer region (although small ripples due to Gibbs' phenomenon [28, page 515] give the mottled appearance in the outer regions of both diagrams). In the inner region, $\bar{\rho}$ falls to the value $-(D - 1)$, as required by the condition (54). Between these zones is a narrow interfacial region in which $\bar{\rho}$ makes a rapid but smooth transition from one value to the other.

At the early time $t = 2$, it is clear from Figure 3 that there is very good agreement between the viscous and inviscid results, as to the location of the interface. As time develops, however, the situation is less clear, although a

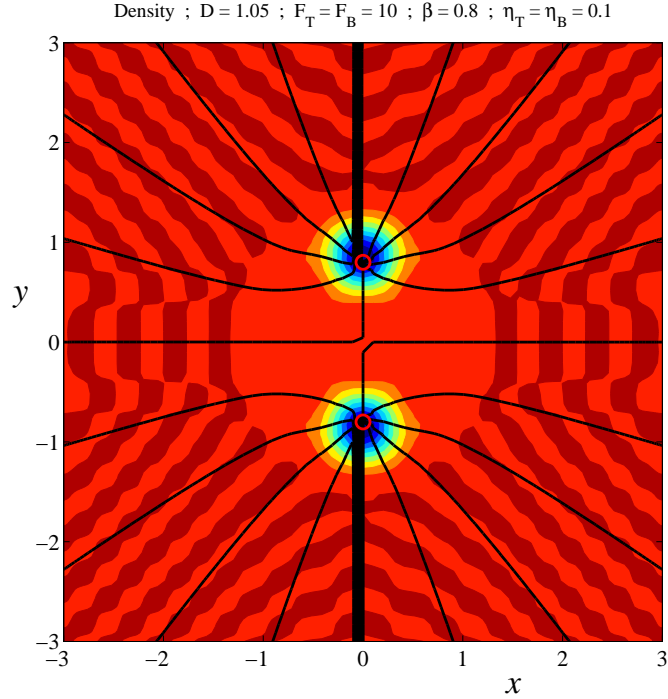


Figure 4: Density contours for the viscous Boussinesq solution, at the time $t = 10$. The streamlines at this time are overlaid on these contours, and are indicated with solid (black) lines. Here, $D = 1.05$, $F_T = F_B = 10$, $\beta = 0.8$, $\eta_T = \eta_B = 0.1$, and the scales on the axes are equal. The two small red circles indicate the locations of the two sources.

visual inspection of the solution at $t = 10$ in Figure 3 nevertheless suggests that the inviscid interface gives a credible estimate for the location of the corresponding viscous interfacial zone. However, at these later times, the Boussinesq approximation itself becomes somewhat questionable, since it is found that the density perturbation $\bar{\rho}$ forms sharp negative depressions near the locations $(x, y) = (0, \pm\beta)$ of the two sources. In these two regions, the perturbation density $\bar{\rho}$ is approximately -0.9 , which violates the assumptions of Boussinesq theory, that this quantity should be small in comparison to 1. It therefore seems likely that a full viscous solution at this later time may differ from this current one based on Boussinesq theory, at least near the two outflow points, and this awaits a future study.

The viscous solution at time $t = 10$ is shown again in Figure 4, as contours of the density perturbation function $\bar{\rho}$. This is the same as the second diagram in Figure 3 except that some streamlines have been overlaid on this

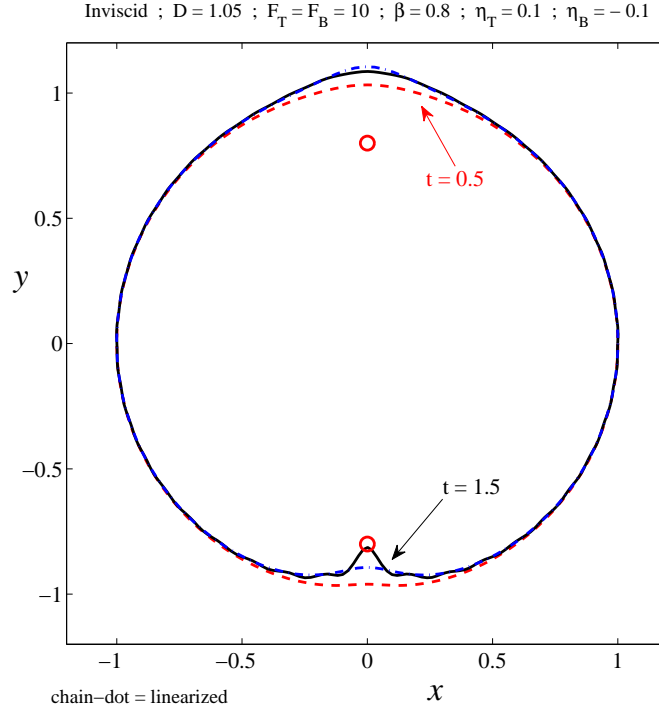


Figure 5: The non-linear inviscid solution for two different times $t = 0.5$ and $t = 1.5$. The linearized interface at time $t = 1.5$ is also shown as a blue chain-dot line. Here, $D = 1.05$, $F_T = F_B = 10$, $\beta = 0.8$, $\eta_T = 0.1$ and $\eta_B = -0.1$, and the scales on the two axes are equal. The two small red circles indicate the locations of the source (top) and sink (bottom).

image. These streamlines are calculated as contours of the streamfunction Ψ in the representation (44), and the solution is shown only over the region $-3 < x < 3$, $-3 < y < 3$ for ease of viewing. Clearly the logarithmic singularities at the two source points $(x, y) = (0, \pm\beta)$ are the dominant features of the flow behaviour, and indeed there is no appreciable change to the streamline pattern over very different times. As expected, the flow field is top-bottom symmetric about the streamline $\Psi = 0$ that lies along the x -axis; it also bifurcates at the origin, and lies also along the portion of the y -axis $-\beta < y < \beta$ connecting the two sources, which are shown with small circles on this diagram.

It is of interest now to examine the converse situation in which one singularity is a source and the other a sink. To achieve this, the top one at $(x, y) = (0, \beta)$ is taken to be a source of strength $\eta_T = 0.1$ while the bottom singularity at $(0, -\beta)$ is a sink, with strength $\eta_B = -0.1$. It should

be recalled, however, that the labels “top” and “bottom” are used purely for convenience to describe the diagrams, since the only actual gravitational attraction in this problem is the force directed radially inward towards each of the two singularities.

The interface $r = \mathcal{R}(\theta, t)$ computed using the non-linear inviscid solution of section 2 is shown in Figure 5, for the two different times $t = 0.5$ and $t = 1.5$. The algorithm fails for times $t > 1.5$, and the physical reason for this is evident from Figure 5. Near the sink at $(0, -\beta)$, the interface is progressively drawn in towards this singularity as time advances. In fact, the interfacial curvature κ is also monitored in this calculation, and the spectral method of section 2 permits it to be computed to high accuracy from the formula

$$\kappa = \frac{2\mathcal{R}_\theta^2 - \mathcal{R}\mathcal{R}_{\theta\theta} + \mathcal{R}^2}{[\mathcal{R}_\theta^2 + \mathcal{R}^2]^{3/2}}, \quad (56)$$

which is given for example, in the text by Anton [29, page 785]. The subscripts denote partial derivatives. As time progresses, the magnitude of the curvature computed from equation (56) steadily increases at the point on the interface closest to the line sink at $(0, -\beta)$, and at the last time $t = 1.5$ for which the algorithm can yield a solution, the curvature forms a large spike at this point. Evidently a curvature singularity will ultimately form at the interface, reminiscent of the Moore singularity [4] in Kelvin-Helmholtz flow, and the effects of this are visible in Figure 5 as the interface forms a cusp as it is drawn into the line sink. The linearized interface computed from equation (30) at this last time $t = 1.5$ is also shown in Figure 5, and is drawn as a chain-dot line. Interestingly, it agrees closely with the non-linear result at this same time almost everywhere, except in the two small regions near each pole; in particular, it cannot predict the sharp inward-facing cusp at the bottom of the diagram, that is associated with the incipient curvature singularity, and this is to be expected.

The Boussinesq viscous solution for this same case is illustrated in Figure 6. Contours of the density perturbation function $\bar{\rho}$ are shown; again, the function is approximately zero in the outer region, apart from small oscillations related to Gibbs’ phenomenon, and these are responsible for the mottled appearance of the background. There is a narrow viscous interfacial region in which the density function $\bar{\rho}$ drops rapidly but smoothly to its interior value $-(D - 1)$. The non-linear inviscid interface at this same time $t = 1.5$ (shown previously in Figure 5) is also drawn on this diagram, as a heavy dashed line. Although this was the largest time for which the non-linear interface could be found, it is clear from Figure 6 that the inviscid solution nevertheless gives a very good estimate of the location of the viscous

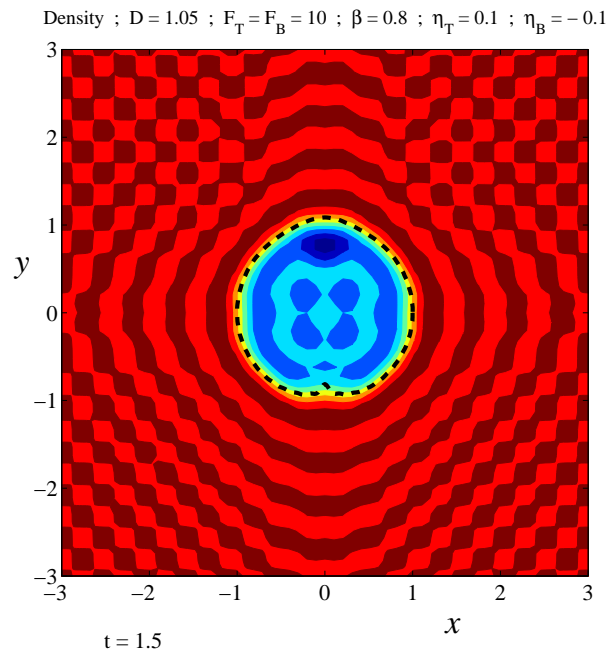


Figure 6: Density contours for the viscous Boussinesq solution, at the time $t = 1.5$. The non-linear inviscid solution is overlaid on this diagram, and is indicated with a heavy dashed line. Here, $D = 1.05$, $F_T = F_B = 10$, $\beta = 0.8$, $\eta_T = 0.1$, $\eta_B = -0.1$, and the scales on the axes are equal.

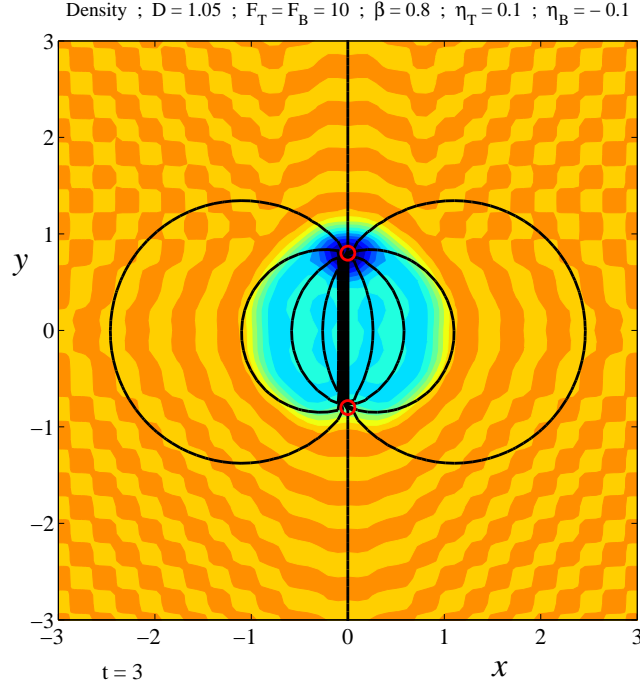


Figure 7: Density contours for the viscous Boussinesq solution, at the time $t = 3$. The streamlines at this time are overlaid on these contours, and are indicated with solid (black) lines. Here, $D = 1.05$, $F_T = F_B = 10$, $\beta = 0.8$, $\eta_T = 0.1$, $\eta_B = -0.1$, and the scales on the axes are equal. The two small red circles indicate the locations of the source and the sink.

interfacial zone in this case.

The viscous solution is capable of continuing to much later times than the non-linear inviscid solution, since it is not limited by the formation of an interfacial cusp and consequent curvature singularity, as occurs in the inviscid case. Figure 7 shows the Boussinesq viscous solution at the substantially later time $t = 3$. Here, contours of the density perturbation function $\bar{\rho}$ are shown, and the viscous interfacial zone dividing the inner and outer fluid regions is clearly visible. In the outer region, $\rho \approx 1$ and inside the interface $\rho \approx 0.95$, as expected for this case $D = 1.05$. However, near the upper singularity at $y = \beta = 0.8$, there is a small region where the density drops to about $\rho \approx 0.9$, and this is visible in Figure 7 as a small dark (blue) region near the source. As time continues, the density drop becomes more pronounced near this point, and eventually a time is reached at which the assumption $|\bar{\rho}| \ll \rho$, inherent in the Boussinesq approximation, becomes invalid. Thus the Boussinesq approximation itself ceases to be appropriate for large enough

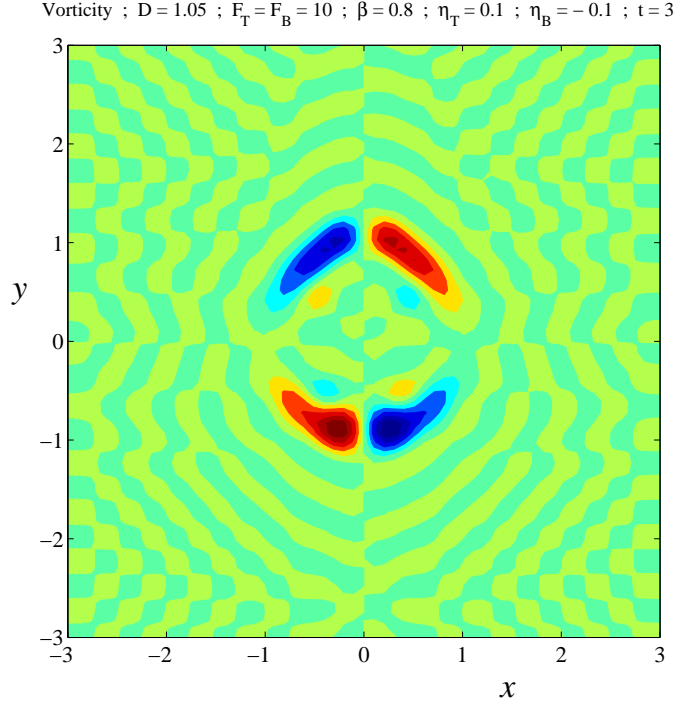


Figure 8: Vorticity contours for the viscous Boussinesq solution, at the time $t = 3$. Here, $D = 1.05$, $F_T = F_B = 10$, $\beta = 0.8$, $\eta_T = 0.1$, $\eta_B = -0.1$, and the scales on the axes are equal.

times, and a more complete description of fully viscous flow would be needed.

The streamline pattern at this time $t = 3$ is also overlaid on the density contours in Figure 7, and is shown using solid (black) lines. It has been calculated using the series representation (44), although it is clearly dominated by the behaviour near the two singularities. Thus the streamlines in Figure 7 have the dipole-like appearance of a standard source-sink pair.

It is of interest to consider briefly the behaviour of the vorticity ζ in this case, and this is done in Figure 8 for the same solution as in Figure 7, at the time $t = 3$. For ease of viewing, only the portion of the solution over the region $-3 < x < 3$, $-3 < y < 3$ is shown, and the function is computed from its spectral representation (45). For a purely inviscid solution, the vorticity ζ would be identically zero everywhere outside the two line singularities, and so this quantity gives a direct measure of the effects of viscosity on the solution. It is found that the vorticity is essentially zero over the entire flow field, much as for the inviscid case, except for the viscous interfacial zone; thus, the vorticity is concentrated in a narrow loop surrounding the inner

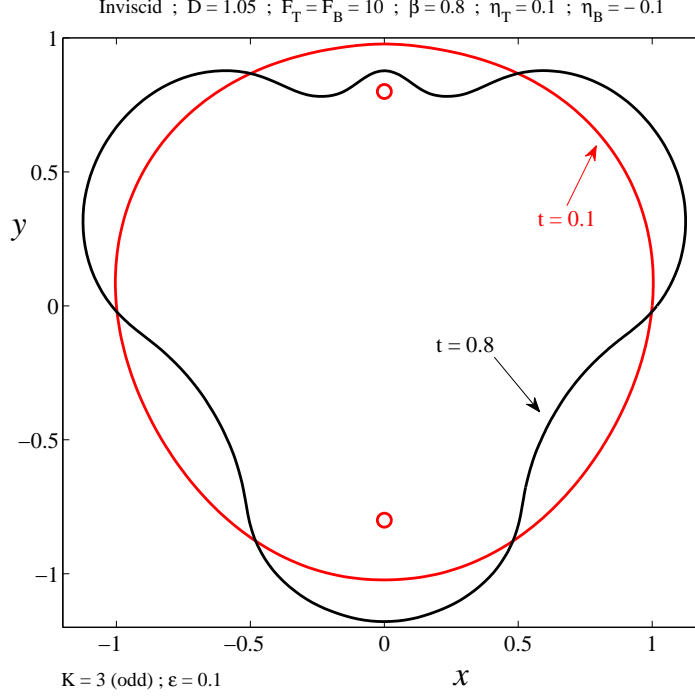


Figure 9: The non-linear inviscid solution for two different times $t = 0.1$ and $t = 0.8$. The initial speed has been perturbed at the third odd radial mode $K = 3$ with amplitude $\epsilon = 0.1$. Here, $D = 1.05$, $F_T = F_B = 10$, $\beta = 0.8$, $\eta_T = 0.1$ and $\eta_B = -0.1$, and the scales on the two axes are equal. The two small red circles indicate the locations of the source (top) and sink (bottom).

fluid zone. This is consistent with what was observed previously by Forbes [9] for planar Rayleigh-Taylor flow. As time progresses, the vorticity in the present problem focusses increasingly at the interfacial zones closest to the two singularities, and this is evident from Figure 8.

Since these flows are unstable in the Rayleigh-Taylor sense, with the outer fluid taken to be more dense than the inner one, it is to be expected that they will be unstable. Accordingly, perturbations made to the initial state may be expected to grow with time. This is explored in Figure 9. Here, two interface shapes are given at the two times $t = 0.1$ and $t = 0.8$, and for exactly the same set of parameter values as those used in Figure 5. However, in Figure 9, a perturbation was made to the initial velocity, and the subsequent different evolution of the solutions in Figures 5 and 9 is due entirely to that fact.

Suppose an initial perturbation is made only to the K -th radial inviscid mode, in equations (7) and (8). Then the radial velocity component in each

fluid would be calculated from the first equation in (2) to give

$$\begin{aligned}
u_1(r, \theta, 0) &= \frac{\eta_T}{2\pi} \frac{(r - \beta \sin \theta)}{(r^2 - 2\beta r \sin \theta + \beta^2)} \\
&+ \frac{\eta_B}{2\pi} \frac{(r + \beta \sin \theta)}{(r^2 + 2\beta r \sin \theta + \beta^2)} \\
&+ \epsilon K r^{K-1} \cos(K\theta), \quad \text{if } r < 1 \\
u_2(r, \theta, 0) &= \frac{\eta_T}{2\pi} \frac{(r - \beta \sin \theta)}{(r^2 - 2\beta r \sin \theta + \beta^2)} \\
&+ \frac{\eta_B}{2\pi} \frac{(r + \beta \sin \theta)}{(r^2 + 2\beta r \sin \theta + \beta^2)} \\
&+ \epsilon K r^{-K-1} \cos(K\theta), \quad \text{if } r > 1.
\end{aligned} \tag{57}$$

These equations (57) represent a perturbation of the *even* K -Fourier mode, and are achieved in the inviscid case simply by setting $P_{1,K} = \epsilon$, $P_{2,K} = -\epsilon$ in the initial conditions; note this is entirely consistent with the linearized solution (24). The corresponding *odd* perturbation is produced at the K -th Fourier mode by replacing the terms $\cos(K\theta)$ with $\sin(K\theta)$ in equation (57), and this initial condition is similarly generated by setting $Q_{1,K} = \epsilon$, $Q_{2,K} = -\epsilon$ at time $t = 0$.

The solution in Figure 9 was achieved with an initial perturbation $K = 3$ at the third odd radial Fourier mode, with amplitude $\epsilon = 0.1$. At time $t = 0$, the interface is originally a circle of unit radius, and the velocity was started from the initial configuration $Q_{1,3} = \epsilon$, $Q_{2,3} = -\epsilon$ with amplitude $\epsilon = 0.1$. By the first time $t = 0.1$ shown in Figure 9, the third mode distortion is weakly visible. This mode continues to develop, and the last time for which the algorithm of section 2 converges is $t = 0.8$, and this final configuration is also shown in Figure 9. The third-mode distortion is by now very strong. When the curvature is examined for the interface at this time, using equation (56), it is found that the portion closest to the upper singularity at $(x, y) = (0, \beta)$ contains a large spike. Evidently a curvature singularity forms at the interface, above this upper source, for some time slightly larger than $t = 0.8$, analogously to the result of Moore [4]. This accounts for the failure of the algorithm for times larger than that shown in Figure 9.

The Boussinesq viscous solution may also be started with the perturbed initial velocity, precisely as for the inviscid solution. The radial outflow in equation (57), and the corresponding component in the azimuthal θ -direction, are used to represent this radial perturbation at the K -th mode in purely

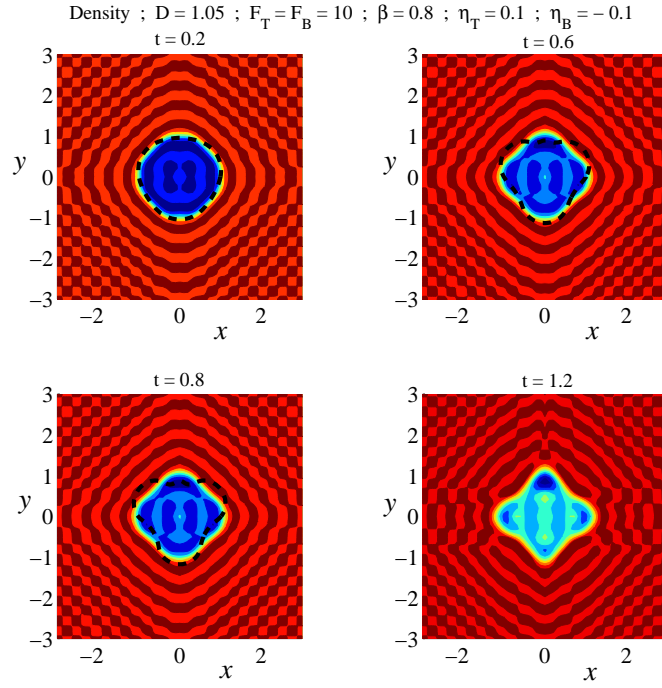


Figure 10: Density contours for the viscous Boussinesq solution, at the times $t = 0.2$, $t = 0.6$ and $t = 0.8$, $t = 1.2$. An initial perturbation of amplitude $\epsilon = 0.1$ was made to the third odd radial mode, $K = 3$. The non-linear inviscid solution is shown for the first three times using a heavy dashed line overlaid on the diagram. Here, $D = 1.05$, $F_T = F_B = 10$, $\beta = 0.8$, $\eta_T = 0.1$, $\eta_B = -0.1$, and the scales on the axes are equal.

cartesian coordinates. The x -component of the perturbed contribution to the velocity may then be written

$$u_C^E(x, y, 0) = \begin{cases} \epsilon K r^{K-1} \cos((K-1)\theta), & \text{if } r < 1 \\ \epsilon K r^{-K-1} \cos((K+1)\theta), & \text{if } r > 1, \end{cases} \quad (58)$$

for a perturbation to the K -th even mode. The odd mode $u_C^O(x, y, 0)$ at the same radial order K is obtained by replacing the two cosine terms in (58) with sine functions. This horizontal velocity component is now compared with the Fourier-series representation obtained by differentiating the streamfunction (44) according to the relations (38). The orthogonality relations for the trigonometric basis functions then yield

$$A_{mn} = \frac{2}{n\pi L} \int_{-L}^L \int_{-B}^B u_C^E(x, y, 0) \sin\left(\frac{m\pi(x+L)}{2L}\right) \cos\left(\frac{n\pi(y+B)}{2B}\right) dy dx$$

$$m = 1, \dots, M, \quad n = 1, \dots, N \quad (59)$$

as the appropriate initial conditions for these Fourier coefficients. The odd-mode coefficients are obtained by replacing $u_C^E(x, y, 0)$ with $u_C^O(x, y, 0)$ in this formula. The integrals in equation (59) are evaluated using Gauss-Legendre quadrature and the routine of von Winckel [27], as previously.

Figure 10 shows the Boussinesq viscous solution for the same situation as illustrated in Figure 9. An initial perturbation of amplitude $\epsilon = 0.1$ has been made to the third odd mode, $K = 3$, and the coefficients then computed numerically from the odd-mode equivalent of equation (59). In these diagrams, contours are shown for the perturbed density function $\bar{\rho}$ computed from its series representation (47). In each of these diagrams, the viscous interfacial region is clearly visible, and corresponds to the narrow zone across which the density changes rapidly but smoothly.

The inviscid non-linear solution is also overlaid on the density contours in Figure 10, for the first three times $t = 0.2, 0.6$ and 0.8 shown. Beyond this last time, the inviscid solution fails to converge due to the formation of a curvature singularity on the interface, near the top source point, as seen previously in Figure 9. At early times, there is reasonable agreement between the predictions of the inviscid theory and the location of the interfacial zone for the viscous model, and this is evident in the first diagram at time $t = 0.2$ in Figure 10. However, in the viscous solution, the source at $y = \beta = 0.8$ and the sink at $y = -\beta = -0.8$ soon begin to dominate the flow, creating a diamond-shaped interfacial zone. As time progresses, this becomes increasingly dissimilar to the inviscid result, and this is due to the vorticity that is generated in the interfacial zone, in the viscous solution. The final diagram

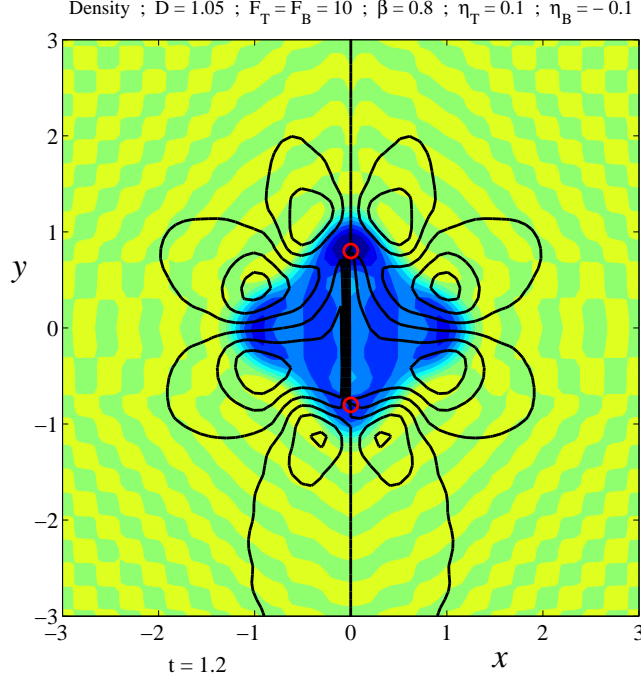


Figure 11: Density contours for the viscous Boussinesq solution, at the time $t = 1.2$, for a solution started with a perturbation at the odd third mode, $K = 3$ with amplitude $\epsilon = 0.1$. The streamlines at this time are overlaid on these contours, and are indicated with solid (black) lines. Here, $D = 1.05$, $F_T = F_B = 10$, $\beta = 0.8$, $\eta_T = 0.1$, $\eta_B = -0.1$, and the scales on the axes are equal. The two small red circles indicate the locations of the source and the sink.

shown in Figure 10, at time $t = 1.2$, shows strongly an elongated interface with a significant outflow near the source at $y = \beta$. There is no corresponding inviscid solution for this time.

The solution at time $t = 1.2$ from Figure 10 is shown again in Figure 11. The diamond-shaped viscous interfacial zone is again clearly visible, and the locations of the source and sink at $y = \pm\beta$ are indicated on this diagram with two small circles. In addition, the streamline pattern at this same time, computed from the representation (44), is overlaid on the figure and illustrated with solid (black) lines. It is interesting to contrast this Figure 11 with the situation in Figure 7, recalling that both pictures were generated using the same parameter values. The only difference between the two occurred in their respective initial conditions; the density profiles and streamlines in Figure 7 represent a solution started purely from the velocity

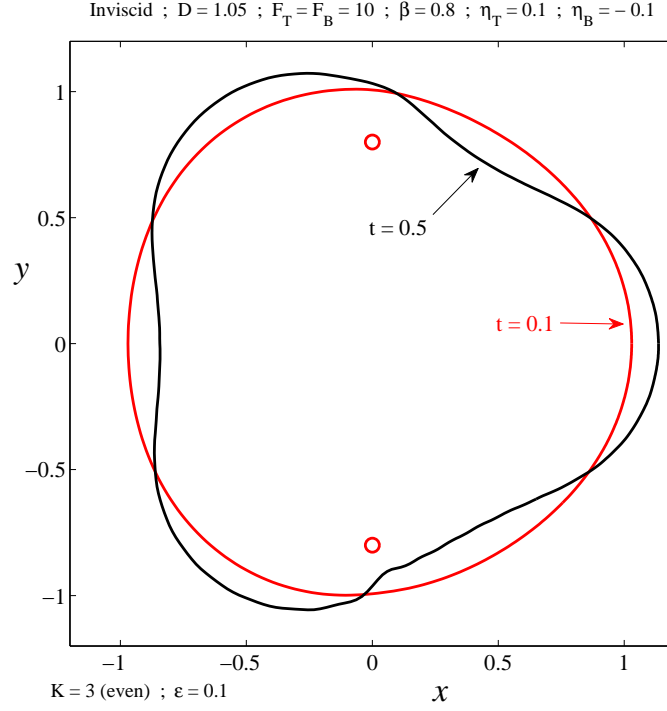


Figure 12: The non-linear inviscid solution for two different times $t = 0.1$ and $t = 0.5$. The initial speed has been perturbed at the third even radial mode $K = 3$ with amplitude $\epsilon = 0.1$. Here, $D = 1.05$, $F_T = F_B = 10$, $\beta = 0.8$, $\eta_T = 0.1$ and $\eta_B = -0.1$, and the scales on the two axes are equal. The two small red circles indicate the locations of the source (top) and sink (bottom).

state determined from the source and the sink, whereas those in Figure 11 resulted from a small perturbation to the odd third radial Fourier mode at the initial time $t = 0$. As a result, the streamline pattern in the unperturbed case in Figure 7 is dominated by the source and sink pair, whereas the streamlines in the perturbed case in Figure 11 are considerably more complicated. In this case, vorticity has clearly been generated at the viscous interfacial zone, and is responsible for the presence of several vortices located around the region. As a result, the streamlines clearly show several looped regions that indicate the locations of these vortices. As a check, the vorticity for this case has been computed from its series representation (45); this is not shown here in the interests of space, but clearly confirms the presence of vortices arranged around the interfacial zone, at the same locations as shown by the streamlines in Figure 11.

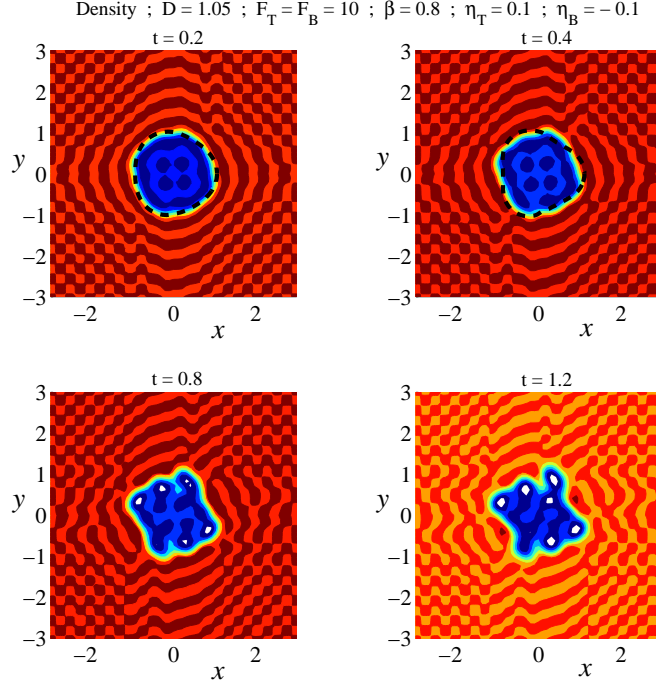


Figure 13: Density contours for the viscous Boussinesq solution, at the times $t = 0.2$, $t = 0.4$ and $t = 0.8$, $t = 1.2$. An initial perturbation of amplitude $\epsilon = 0.1$ was made to the third even radial mode, $K = 3$. The non-linear inviscid solution is shown for the first two times using a heavy dashed line overlaid on the diagram. Here, $D = 1.05$, $F_T = F_B = 10$, $\beta = 0.8$, $\eta_T = 0.1$, $\eta_B = -0.1$, and the scales on the axes are equal.

To conclude this presentation of results, it is of interest to consider the same solution, but now perturbed at the third *even* radial Fourier mode. The inviscid situation is depicted in Figure 12. Once again, the parameters are identical to those in Figures 5 and 9, and only differs from those other two cases in the nature of the initial condition. The behaviour of this non-linear inviscid solution is markedly different to the situation shown in Figure 9. Thus, although there is clearly the unstable growth of a perturbation at the third mode, it is roughly orthogonal to that shown in Figure 9. Eventually, the inviscid solution fails for a time slightly larger than $t = 0.5$, and an examination of the interfacial curvature, calculated from equation (56), shows that now a curvature singularity begins to form at the point on the interface closest to the *sink* at the bottom of the diagram. At this point, the interface evidently develops an inward-facing cusp, as it is eventually drawn in towards the sink.

The corresponding viscous solution is shown in Figure 13. Contours of the density perturbation function $\bar{\rho}$ at the two relatively early times $t = 0.2$ and 0.4 are presented in Figure 13; for these first two times, the non-linear inviscid solution also exists, and the interface predicted by that model is overlaid on each picture, and sketched using a heavy dashed line. There is reasonable agreement between the two at very early times, but the two start to differ markedly as time progresses. Eventually, the inviscid solution fails slightly later than $t = 0.5$, with the formation of a curvature singularity at the interface near the lower sink point, but the non-linear model continues to produce results for later times. Two of these are also presented in Figure 13, for times $t = 0.8$ and $t = 1.2$. It is interesting to contrast these with the corresponding solutions in Figure 10, for the same parameter values and at the same two times, but starting with an odd third-mode perturbation. The *even* perturbation used in Figure 13 produces very differently-shaped outflows, which now have no plane of symmetry and a more elaborate shape.

As for the odd perturbation in Figure 11, the solution at time $t = 1.2$ produced from an *even* initial perturbation is displayed in Figure 14. The viscous interfacial zone is clearly visible in this diagram, and the locations of the source and sink are indicated with small circles. Unlike the odd case discussed earlier, it is evident that the interface in this even case now passes almost directly into these two singularities. In addition, the streamlines for this situation have again been computed from the representation (44) and have been overlaid on the density contours and drawn with heavy dark lines. Their pattern is very different to that shown earlier in Figure 11, and indicates the location of the vortices which are arranged around the interface for this case. Again, the vorticity in this situation has been computed, and while not presented here, it confirms the streamline pattern shown in Figure 14.

6 Discussion and Conclusion

In this paper, viscous and inviscid planar outflow from *two* line sources has been considered. These two sources lie within an inner fluid region in which the fluid is less dense than the surrounding fluid. An interface is present between the two, and it deforms in response to the movement of the fluid produced by the sources. Each source is massive, and so generates its own inwardly-directed gravitational field. The outflow is therefore unstable in a Rayleigh-Taylor sense, since a heavier surrounding fluid is being pushed outwards by the lighter inner fluid. As a result, the shape of the interface is evidently strongly influenced by the initial conditions for the flow, even in

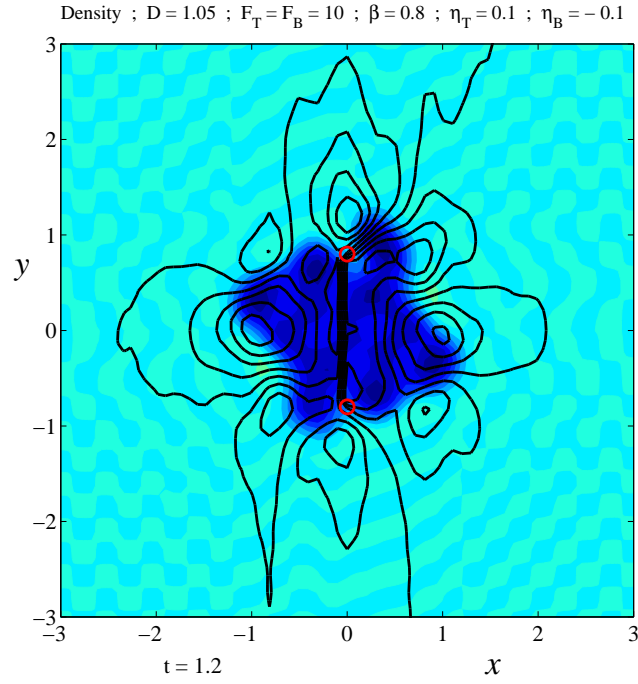


Figure 14: Density contours for the viscous Boussinesq solution, at the time $t = 1.2$, for a solution started with a perturbation at the even third mode, $K = 3$ with amplitude $\epsilon = 0.1$. The streamlines at this time are overlaid on these contours, and are indicated with solid (black) lines. Here, $D = 1.05$, $F_T = F_B = 10$, $\beta = 0.8$, $\eta_T = 0.1$, $\eta_B = -0.1$, and the scales on the axes are equal. The two small red circles indicate the locations of the source and the sink.

the presence of the two sources.

A linearized solution has been developed for the inviscid model, under the assumption that the interface remains approximately circular throughout its evolution. It has been shown that the flow experienced by the inner fluid is equivalent to one in which there are image sources located at the inverse distances of the actual sources from the origin, being thus situated within the surrounding outer fluid. For the fluid outside the interface, there are likewise equivalent image sources, and these are positioned at the locations of the two actual sources within the inner fluid. An elegant closed-form expression is obtained for the interface shape within the early period of its growth; it agrees well with the numerically obtained non-linear inviscid solution at early times, but eventually the two differ significantly, since the key linearizing assumption, that the interface remains roughly circular, fails to hold true for later times. This is to be expected.

Non-linear inviscid solutions are computed to very high accuracy using a modification of the spectral method originally proposed by Forbes, Chen and Trenham [24]. In every case examined, it has been found that the solution eventually fails beyond some critical time, at which a curvature singularity is evidently formed at the interface. A similar situation was encountered by Forbes [19] in a study of radial Rayleigh-Taylor flow, and is consistent with the original work of Moore [4]. Where, precisely, the curvature singularity forms is sensitively dependent on the initial conditions for the flow. When one of the sources has negative strength, and so becomes a sink, it is often observed that the singularity at the interface forms near that sink; this agrees with intuition, which suggests that the interface might be drawn inwards toward the sink, and eventually form a cusp, at which the curvature becomes infinite. However, there are some initial conditions for which the curvature singularity forms close to the source, and one such instance has been shown in Figure 9.

Viscous solutions have also been presented, using the Boussinesq approximation to replace the true viscous interface with a region in which the fluid density changes rapidly but smoothly from its inner value to the density of the outer fluid. A new spectral method has been developed, to account for the presence of *multiple* singularities within the fluid. The governing equations are first multiplied by the terms required to cancel the singular behaviour at the sources, and then spectrally decomposed. Necessarily this means that the orthogonality of the basis functions cannot be used to give simple differential equations for the Fourier coefficients, and a matrix equation must instead be solved for the derivatives of these coefficients at each time step. However, the coefficient matrix is time-independent, and so can be computed once at the beginning of the algorithm, stored, and not recalculated. As a result, the

algorithm retains its numerical efficiency. In fact, it has also been found that caching the basis functions in the representations (44), (47) at the beginning of the procedure also leads to a great reduction in computer run time.

The Boussinesq viscous solutions are found to agree well with the non-linear inviscid solutions at early times, and this fact gives confidence in the results. However, as time progresses, the two sets of results may diverge, and this may be due to different physically-based causes. Firstly, the inviscid solution ultimately fails because the interface develops a curvature singularity at some finite critical time. This is consistent with the discovery of a similar effect in Kelvin-Helmholtz (shear) flows by Moore [4]. Viscous solutions do not experience such singular behaviour, in part because their interfacial zone is of finite width, rather than occurring as a singular mathematical line, and also because they have the capacity to generate vorticity at the interface, which is impossible in the inviscid solution. Indeed, Forbes [9] observed numerically that, in a viscous Boussinesq solution of the classical planar Rayleigh-Taylor problem, the viscous solution placed a small intense region of vorticity at precisely the time and location at which the corresponding inviscid solution sought to generate a curvature singularity. A second factor affecting the evolution of the viscous interface is the possible formation of vortices around the interfacial zone; their number and location is strongly influenced by initial conditions.

A large number of solutions has been generated in the course of this study, although most are not presented here. Unlike the case of a single line source studied by Forbes [19], overturning plumes forming mushroom-cloud like structures have not been obtained here. Care has been taken in this paper to ensure that the viscous solutions shown conform to the basic premise of Boussinesq theory, namely, that the density perturbation should remain small relative to the background density; in the present dimensionless variables, this condition reduces to $|\bar{\rho}| \ll 1$. Nevertheless, there are many situations in which this basic requirement ceases to hold. One such example concerns the case when the two sources differ very markedly in strength; in that case, a time is soon reached at which the density near one of the sources evidently forms a large spike, reminiscent of a Dirac delta function. Clearly such a situation violates the requirement of a small perturbation density, and so it must be the case that Boussinesq theory will fail to be valid in such circumstances, after a certain time. At present, it is unclear what a more complete viscous solution might give, and that remains a topic for future study. In addition, Lee and Kim [30] have pointed out that Boussinesq theory, as applied by Forbes [9] to planar Rayleigh-Taylor flow, is deficient in the sense that it always predicts rising bubbles and falling drips that are symmetrical about the undisturbed surface, while more complete viscous

models and experiments do not always confirm this prediction. Thus a more exact viscous theory may yet generate further interesting outcomes in this problem, but must be left for future study.

Acknowledgements: This work has been carried out in association with Australian Research Council grant DP140100094.

References

- [1] Rayleigh, Lord, Investigation of the character of the equilibrium of an incompressible heavy fluid of variable density. *Proc. London Math. Soc.*, **14** (1883) 170–177.
- [2] Taylor, Sir G.I., The instability of liquid surfaces when accelerated in a direction perpendicular to their planes, I. *Proc. Roy. Soc. London Ser. A*, **201** (1950) 192–196.
- [3] Sharp, D.H., An overview of Rayleigh-Taylor instability. *Physica D*, **12** (1984) 3–18.
- [4] Moore, D.W., The spontaneous appearance of a singularity in the shape of an evolving vortex sheet. *Proc. Roy. Soc. London Ser. A*, **365** (1979) 105–119.
- [5] Cowley, S.J., Baker, G.R. and Tanveer, S., On the formation of Moore curvature singularities in vortex sheets. *J. Fluid Mech.*, **378** (1999) 233–267.
- [6] Baker, G., Caffisch, R.E. and Siegel M., Singularity formation during Rayleigh-Taylor instability. *J. Fluid Mech.*, **252** (1993) 51–78.
- [7] Krasny, R., Desingularization of periodic vortex sheet roll-up. *J. Comput. Phys.*, **65** (1986) 292–313.
- [8] Baker, G.R. and Pham, L.D., A comparison of blob-methods for vortex sheet roll-up. *J. Fluid Mech.*, **547** (2006) 297–316.
- [9] Forbes, L.K., The Rayleigh-Taylor instability for inviscid and viscous fluids. *J. Engin. Math.*, **65** (2009) 273–290.
- [10] Kelley, M.C., Dao, E., Kuranz, C. and Stenbaek-Nielsen, H., Similarity of Rayleigh-Taylor Instability development on scales from 1mm to One Light Year. *Int. J. Astron. Astrophys.*, **1** (2011) 173–176.

- [11] Kull, H.J., Theory of the Rayleigh-Taylor instability. *Phys. Lett.*, **206** (1991) 197–325.
- [12] Inogamov, N.A., The role of Rayleigh-Taylor and Richtmyer-Meshkov instabilities in astrophysics: an introduction. *Astrophys. Space Phys.*, **10** (1999) 1–335.
- [13] Waddell, J.T., Niederhaus, C.E. and Jacobs, J.W., Experimental study of Rayleigh-Taylor Instability: Low Atwood number liquid systems with single-mode initial perturbations. *Phys. Fluids*, **13** (2001) 1263–1273.
- [14] McClure-Griffiths, N.M., Dickey, J.M., Gaensler, B.M. and Green, A.J., Loops, drips, and walls in the galactic chimney GSH 277 + 00 + 36. *Astrophys. J.*, **594** (2003) 833–843.
- [15] Low, M.-M. M. and McCray, R., Superbubbles in disk galaxies. *Astrophys. J.*, **324** (1988) 776–785.
- [16] Epstein, R., On the Bell-Plesset effects: The effects of uniform compression and geometrical convergence on the classical Rayleigh-Taylor instability. *Phys. Plasmas*, **11** (2004) 5114–5124.
- [17] Mikaelian, K.O., Rayleigh-Taylor and Richtmyer-Meshkov instabilities and mixing in stratified cylindrical shells. *Phys. Fluids*, **17**, 094105 (2005) 13 pages.
- [18] Yu, H. and Livescu, D., Rayleigh-Taylor instability in cylindrical geometry with compressible fluids. *Phys. Fluids*, **20**, 104103 (2008) 11 pages.
- [19] Forbes, L.K., A cylindrical Rayleigh-Taylor instability: radial outflow from pipes or stars. *J. Engin. Math.*, **70** (2011a) 205–224.
- [20] Matsuoka, C. and Nishihara, K., Analytical and numerical study on a vortex sheet in incompressible Richtmyer-Meshkov instability in cylindrical geometry. *Phys. Rev. E*, **74**, 066303 (2006) 12 pages.
- [21] Forbes, L.K., Rayleigh-Taylor instabilities in axi-symmetric outflow from a point source. *ANZIAM J.*, **53** (2011b) 87–121.
- [22] Gómez, L., Rodríguez, L.F. and Loinard, L., A one-sided knot ejection at the core of the HH 111 outflow. *Revista Mexicana Astron. Astro.*, **49** (2013) 79–85.
- [23] Stahler, S.W. and Palla, F., *The Formation of Stars*. Wiley - VCH, Berlin (2004).

- [24] Forbes, L.K., Chen, M.J. and Trenham C.E., Computing unstable periodic waves at the interface of two inviscid fluids in uniform vertical flow. *J. Comput. Phys.*, **221** (2007) 269–287.
- [25] Farrow, D.E. and Hocking G.C., A numerical model for withdrawal from a two-layer fluid. *J. Fluid Mech.*, **549** (2006) 141–157.
- [26] Batchelor, G.K., *An Introduction to Fluid Dynamics*. Cambridge University Press, Cambridge (1967).
- [27] von Winckel, G., *lgwt.m*, at: MATLAB file exchange website, written (2004). <http://www.mathworks.com/matlabcentral/fileexchange/loadFile.do?objectId=4540&objectType=file>
- [28] Kreyszig, E., *Advanced Engineering Mathematics, tenth edition*. Wiley, New York (2011).
- [29] Anton, H., *Calculus with analytic geometry*. Wiley, New York (1980).
- [30] Lee, H.G. and Kim, J., A comparison study of the Boussinesq and the variable density models on buoyancy-driven flows. *J. Engin. Math.*, **75** (2012) 15–27.
- [31] Saff, E.B. and Snider, A.D., *Fundamentals of Complex Analysis for Mathematics, Science and Engineering*. Prentice-Hall, New Jersey (1976).

7 Appendix

In this Appendix, the integrals defining the constants $\mathcal{C}_n(\beta)$ and $\mathcal{S}_n(\beta)$ in equation (28) are calculated in closed form, using the calculus of residues. For convenience, attention is focussed purely on the two integrals in these definitions, which are written here as

$$\begin{aligned} K_n(\beta) &= \int_{-\pi}^{\pi} \frac{\cos \theta \sin(n\theta)}{1 - 2\beta \sin \theta + \beta^2} d\theta \\ L_n(\beta) &= \int_{-\pi}^{\pi} \frac{\cos \theta \cos(n\theta)}{1 - 2\beta \sin \theta + \beta^2} d\theta. \end{aligned} \quad (60)$$

These are converted into contour integrals in a complex z -plane, in the standard manner (see Saff and Snider [31, section 6.2]). The integrals can be regarded as describing a single revolution on the unit circle $|z| = 1$,

parametrized as $z = \exp(i\theta)$. The two trigonometric functions are eliminated according to the formulae

$$\cos \theta = \frac{1}{2} \left(z + \frac{1}{z} \right) \quad ; \quad \sin \theta = \frac{1}{2i} \left(z - \frac{1}{z} \right),$$

and the terms in equation (60) are expressed as

$$\begin{aligned} K_n(\beta) &= \frac{i}{4\beta} \left[J_1 - J_2 + J_3 - J_4 \right] \\ L_n(\beta) &= -\frac{1}{4\beta} \left[J_1 + J_2 + J_3 + J_4 \right]. \end{aligned} \quad (61)$$

In this expression, the four terms

$$\begin{aligned} J_1 &= \oint \frac{z^{n+1}}{(z - i\beta)(z - i/\beta)} dz \\ J_2 &= \oint \frac{z^{1-n}}{(z - i\beta)(z - i/\beta)} dz \\ J_3 &= \oint \frac{z^{n-1}}{(z - i\beta)(z - i/\beta)} dz \\ J_4 &= \oint \frac{z^{-n-1}}{(z - i\beta)(z - i/\beta)} dz \end{aligned} \quad (62)$$

have been defined for convenience. Each of them is a contour integral about the unit circle traversed once in the positive direction, as illustrated in Figure 15.

The two terms J_1 and J_3 appearing in equations (62) are straightforward to evaluate, since they each only contain a simple pole at the single point $z = i\beta$ within the unit circle (since $\beta < 1$). The residue at this point is easily obtained, and it follows that

$$\begin{aligned} J_1 &= 2\pi(i^{n+1}) \frac{\beta^{n+2}}{(\beta^2 - 1)} \\ J_3 &= 2\pi(i^{n-1}) \frac{\beta^n}{(\beta^2 - 1)}. \end{aligned} \quad (63)$$

The integrand of the term J_2 in equation (62) has both a simple pole at $z = i\beta$ as well as a pole of order $n - 1$ at the origin $z = 0$. The residue of the simple pole is easy to calculate, but that of the high-order pole at the

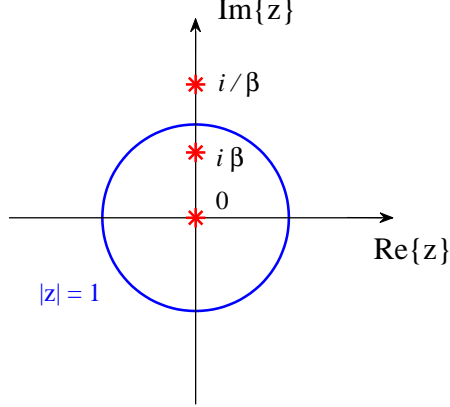


Figure 15: The contour used in the complex plane, along which the integrals in equations (62) are evaluated. The (red) stars denote the possible locations of pole singularities.

origin is more difficult. It is appropriate to use partial fractions to re-write this expression as

$$J_2 = \frac{\beta}{i(\beta^2 - 1)} \oint \frac{1}{z^{n-1}} \left[\frac{1}{z - i\beta} - \frac{1}{z - i/\beta} \right] dz.$$

In this form, the residue of the pole of order $n - 1$ at the origin may now be obtained by differentiation, and a little algebra gives the simple final form

$$J_2 = 2\pi(i^{1-n}) \frac{\beta^n}{(\beta^2 - 1)}. \quad (64)$$

A similar use of partial fractions is applied to the expression for J_4 in (62), since it too involves a simple pole at the point $z = i\beta$ and a pole of order $n + 1$ at the origin $z = 0$. This quantity can therefore be calculated to be

$$J_4 = 2\pi \frac{\beta^{n+2}}{i^{n+1}(\beta^2 - 1)}. \quad (65)$$

These four expressions in equations (63), (64), (65) are now substituted into the expressions (61) for K_n and L_n , and yield the results

$$\begin{aligned} K_n &= -\pi\beta^{n-1} \cos(n\pi/2) \\ L_n &= \pi\beta^{n-1} \sin(n\pi/2). \end{aligned}$$

These formulae now give the final forms (29) in the text.